

Deep Algorithm Unrolling for Blind Image Deblurring

Yuelong Li, *Student Member, IEEE*, Mohammad Tofighi, *Student Member, IEEE*,
Junyi Geng, *Student Member, IEEE*, Vishal Monga, *Senior Member, IEEE*, and Yonina C. Eldar, *Fellow, IEEE*

Abstract—Blind image deblurring remains a topic of enduring interest. Learning based approaches, especially those that employ neural networks have emerged to complement traditional model based methods and in many cases achieve vastly enhanced performance. That said, neural network approaches are generally empirically designed and the underlying structures are difficult to interpret. In recent years, a promising technique called algorithm unrolling has been developed that has helped connect iterative algorithms such as those for sparse coding to neural network architectures. However, such connections have not been made yet for blind image deblurring. In this paper, we propose a neural network architecture based on this idea. We first present an iterative algorithm that may be considered as a generalization of the traditional total-variation regularization method in the gradient domain. We then unroll the algorithm to construct a neural network for image deblurring which we refer to as Deep Unrolling for Blind Deblurring (DUBLID). Key algorithm parameters are learned with the help of training images. Our proposed deep network DUBLID achieves significant practical performance gains while enjoying interpretability at the same time. Extensive experimental results show that DUBLID outperforms many state-of-the-art methods and in addition is computationally faster.

I. INTRODUCTION

BLIND image deblurring refers to the process of recovering a sharp image from its blurred observation without explicitly knowing the blur function. In real world imaging, images frequently suffer from degraded quality as a consequence of blurring artifacts, which blind deblurring algorithms are designed to remove such artifacts. These artifacts may come from different sources, such as atmospheric turbulence, diffraction, optical defocusing, camera shaking, and more [1]. In the computational imaging literature, motion deblurring is an important topic because camera shakes are common during the photography procedure. In recent years, this topic has attracted growing attention thanks to the popularity of smartphone cameras. On such platforms, the motion deblurring algorithm plays an especially crucial role because effective hardware solutions such as professional camera stabilizers are difficult to deploy due to space restrictions.

In this work we focus on motion deblurring in particular because of its practical importance. However, our development does not make assumptions on blur type and hence may be extended to cases other than motion blur. Motion blurs occur as a consequence of relative movements between the

camera and the imaged scene during exposure. Assuming the scene is planar and the camera motion is translational, the image degradation process may be modelled as a discrete convolution [1]:

$$\mathbf{y} = \mathbf{k} * \mathbf{x} + \mathbf{n}, \quad (1)$$

where \mathbf{y} is the observed blurry image, \mathbf{x} is the latent sharp image, \mathbf{k} is the unknown point spread function (blur kernel), and \mathbf{n} is random noise which is often modelled as Gaussian. Blind motion deblurring corresponds to estimating both \mathbf{k} and \mathbf{x} given \mathbf{y} ; this estimation problem is also commonly called blind deconvolution.

Related Work: The majority of existing blind motion deblurring methods are based on iterative optimization. Early works can be traced back to several decades ago [2], [3], [4], [1], [5]. These methods are only effective when the blur kernel is relatively small. In the last decade, significant breakthroughs have been made both practically and conceptually. As both the image and the kernel need to be estimated, there are infinitely many pairs of solutions forming the same blurred observation rendering blind deconvolution an ill-posed problem. A popular remedy is to add regularizations so that many blind deblurring algorithms essentially reduce to solving regularized inverse problems. A vast majority of these techniques hinge on sparsity-inducing regularizers, either in the gradient domain [6], [7], [8], [9], [10], [11], [12], [13] or more general sparsifying transformation domains [14], [15], [16], [17]. Variants of such methods may arise indirectly from a statistical estimation perspective, e.g. [18], [19], [20], [21].

From a conceptual perspective, Levin *et al.* [22] study the limitations and remedies of the commonly employed Maximum a Posterior (MAP) approach, while Perrone *et al.* [23] extend their study with a particular focus on Total-Variation (TV) regularization. Despite some performance improvements achieved along their developments, the iterative optimization approaches generally suffer from several limitations. First, their performance depends heavily on appropriate selection of parameter values. Second, handcrafted regularizers play an essential role, and designing versatile regularizers that generalize well to a variety of real datasets can be a challenging task. Finally, hundreds and thousands of iterations are often required to reach an acceptable performance level and thus these approaches can be slow in practice.

Complementary to the aforementioned approaches, learning based methods for determining a non-linear mapping that deblurs the image while adapting parameter choices to an underlying training image set have been developed. Principally

Y. Li, M. Tofighi, and V. Monga are with Department of Electrical Engineering, The Pennsylvania State University, University Park, PA, 16802 USA, Emails: yul200@psu.edu, tofighi@psu.edu, vmonga@engr.psu.edu

Y. C. Eldar is with Department of Electrical Engineering, Technion, Israel Institute of Technology, Haifa, Israel, Email: yonina@ee.technion.ac.il

important in this class are techniques that employ deep neural networks. The history of leveraging neural networks for blind deblurring actually dates back to the last century [24]. In the past few years, there has been a growing trend in applying neural networks to various imaging problems [25], and blind motion deblurring has followed that trend. Xu *et al.* [26] use large convolution kernels with carefully chosen initializations in a Convolutional Neural Network (CNN); Yan *et al.* [27] concatenate a classification network with a regression network to deblur images without prior information about the blur kernel type. Chakrabarti *et al.* [28] work in the frequency domain and employ a neural network to predict Fourier transform coefficients of image patches; Xu *et al.* [29] employ a CNN for edge enhancement prior to kernel and image estimation. These works often outperform iterative optimization algorithms especially for linear motion kernels; however, the structures of the networks are often empirically determined and their actual functionality is hard to interpret.

In the seminal work of Gregor *et al.* [30], a novel technique called algorithm unrolling was proposed. Despite its focus on approximating sparse coding algorithms, it provides a principled framework for expressing traditional iterative algorithms as neural networks, and offers promise in developing interpretable network architectures. Specifically, each iteration step may be represented as one layer of the network, and concatenating these layers form a deep neural network. Passing through the network is equivalent to executing the iterative algorithm a finite number of times. The network may be trained using back-propagation [31], and the trained network can be naturally interpreted as a parameter optimized algorithm. An additional benefit is that prior knowledge about the conventional algorithms may be transferred. There has been limited recent exploration of neural network architectures by unrolling iterative algorithms for problems such as super-resolution and clutter/noise suppression [32], [33], [34], [35]. In blind deblurring, Schuler *et al.* [36] employ neural networks as feature extraction modules towards a trainable deblurring system. However, the network portions are still empirical.

Other aspects of deblurring have been investigated such as spatially varying blurs [37], [38], including some recent neural network approaches [39], [40], [41], [42]. Other algorithms benefit from device measurements [43], [44], [45] or leverage multiple images [46], [47].

Motivations and Contributions: Conventional iterative algorithms have the merits of interpretability, but acceptable performance levels demand much longer execution time compared to modern neural network approaches. Despite previous efforts, the link between both categories remains largely unexplored for the problem of blind deblurring, and a method that simultaneously enjoys the benefits of both is lacking. In this regard, we make the following contributions:¹

¹A preliminary 4 page version of this work has been submitted to IEEE ICASSP 2019 [48]. This paper involves substantially more analytical development in the form of: a.) the unrolling mechanism and associated optimization problem for learning parameters, b.) derivation of custom back-propagation rules, c.) handling of color images, and d.) demonstration of computational benefits. Experimentally, we have added a new dataset and several new state of the art methods and scenarios in our comparisons. Finally, ablation studies have been included to better explain the proposed DUBLID and its merits.

- **Deep Unrolling for BLind Deblurring (DUBLID):** We propose an interpretable neural network structure called DUBLID. We first present an iterative algorithm that may be considered a generalization of the traditional total-variation regularization method in the gradient domain, and subsequently unroll the algorithm to construct a neural network. Key algorithm parameters are learned with the help of training images using backpropagation, for which we derive analytically simple forms that are amenable to fast implementation.
- **Performance and Computational Benefits:** Through extensive experimental validation over *three* benchmark datasets, we verify the superior performance of the proposed DUBLID, both over conventional iterative algorithms and more recent neural network approaches. Both traditional linear and more recently developed non-linear kernels are used in our experiments. Besides quality gains, we show that DUBLID is computationally simpler. In particular, the carefully designed interpretable layers enables DUBLID to learn with far fewer parameters than state of the art deep learning approaches – hence leading to much faster inference time.
- **Reproducibility:** To ensure reproducibility, we share our code and datasets that are used to generate all our experimental results freely online.

The rest of the paper is organized as follows. Generalized gradient domain deblurring is reviewed in Section II. We identify the roles of (gradient/feature extraction) filters and other key parameters, which are usually assumed *fixed*. Based on a half-quadratic optimization procedure to solve the aforementioned gradient domain deblurring, we develop a new unrolling method that realizes the iterative optimization as a neural network in Section III. In particular, we show that the various linear and non-linear operators in the optimization can be cascaded to generate an interpretable deep network, such that the number of layers in the network corresponds to the number of iterations. The fixed filters and parameters are now *learnable* and a custom back-propagation procedure is proposed to optimize them based on training images. Experimental results that provide insights into DUBLID as well as comparisons with state of the art methods are reported in Section IV. Section V concludes the paper.

II. GENERALIZED BLIND DEBLURRING VIA ITERATIVE MINIMIZATION: A FILTERED DOMAIN REGULARIZATION PERSPECTIVE

A. Blind Deblurring in the Filtered Domain

A common practice for blind motion deblurring is to estimate the kernel in the image gradient domain [18], [7], [8], [9], [19], [10], [23]. Because the gradient operator ∇ commutes with convolution, taking derivatives on both side of (1) gives

$$\nabla \mathbf{y} = \mathbf{k} * \nabla \mathbf{x} + \mathbf{n}', \quad (2)$$

where $\mathbf{n}' = \nabla \mathbf{n}$ is Gaussian noise. Formulation in the gradient domain, as opposed to the pixel domain, has several desirable strengths: first, the kernel generally serves as a low-pass filter, and low-frequency components of the image are barely

informative about the kernel. Intuitively, the kernel may be inferred along edges rather than homogeneous regions in the image. Therefore, a gradient domain approach can lead to improved performance in practice [19] as the gradient operator effectively filtered out the uninformative regions. Additionally, from a computational perspective, gradient domain formulations help in better conditioning of the linear system resulting in more reliable estimation [8].

The model (2) alone, however, is insufficient for recovering both the image and the kernel; thus regularizers on both are needed. The gradients of natural images are generally sparse, i.e., most of their values are of small magnitude [18], [22]. This fact motivates the developments of various sparsity-inducing regularizations on $\nabla \mathbf{x}$. Among them one of particular interest is the ℓ_1 -norm (often called TV) thanks to its convexity [5], [23]. To regularize the kernel, it is common practice to assume the kernel coefficients are non-negative and of unit sum. Consolidating these facts, blind motion deblurring may be carried out by solving the following optimization problem [23]:

$$\begin{aligned} \min_{\mathbf{k}, \mathbf{g}_1, \mathbf{g}_2} & \frac{1}{2} \left(\|D_x \mathbf{y} - \mathbf{k} * \mathbf{g}_1\|_2^2 + \|D_y \mathbf{y} - \mathbf{k} * \mathbf{g}_2\|_2^2 \right) \\ & + \lambda_1 \|\mathbf{g}_1\|_1 + \lambda_2 \|\mathbf{g}_2\|_1 + \frac{\epsilon}{2} \|\mathbf{k}\|_2^2, \\ \text{subject to } & \|\mathbf{k}\|_1 = 1, \quad \mathbf{k} \geq 0, \end{aligned} \quad (3)$$

where $D_x \mathbf{y}, D_y \mathbf{y}$ are the partial derivatives of \mathbf{y} in horizontal and vertical directions respectively. The notation $\|\cdot\|_p$ denotes the ℓ_p vector norm, while $\lambda_1, \lambda_2, \epsilon$ are positive constant parameters to balance the contributions of each term. The \geq sign is to be interpreted elementwise. The solutions \mathbf{g}_1 and \mathbf{g}_2 of (3) are estimates of the gradients of the sharp image \mathbf{x} , i.e., we may expect $\mathbf{g}_1 \approx D_x \mathbf{x}$ and $\mathbf{g}_2 \approx D_y \mathbf{x}$.

In practice, numerical gradients of images are usually computed using discrete filters, such as the Prewitt and Sobel filters. From this viewpoint, $D_x \mathbf{y}$ and $D_y \mathbf{y}$ may be viewed as filtering \mathbf{y} through two derivative filters of orthogonal directions [49]. Therefore, a straightforward generalization of (3) is to use more than two filters, i.e., pass \mathbf{y} through a filter bank. This generalization increases the flexibility of (3), and appropriate choice of the filters can significantly boost performance. In particular, by steering the filters towards more directions other than horizontal and vertical, local features (such as lines, edges and textures) of different orientations are more effectively captured [50], [51], [52]. Moreover, the filter can adapt its shapes to enhance the representation sparsity [53], [54], a desirable property to pursue.

Suppose we have determined a desired collection of C filters $\{\mathbf{f}_i\}_{i=1}^C$. By commutativity of convolutions, we have

$$\mathbf{f}_i * \mathbf{y} = \mathbf{f}_i * \mathbf{k} * \mathbf{x} + \mathbf{n}'_i = \mathbf{k} * (\mathbf{f}_i * \mathbf{x}) + \mathbf{n}'_i, \quad i = 1, 2, \dots, C, \quad (4)$$

where the filtered noises $\mathbf{n}'_i = \mathbf{f}_i * \mathbf{n}$ are still Gaussian. To encourage sparsity of the filtered image, we formulate the optimization problem (which may similarly be regarded as a generalization of [23])

$$\begin{aligned} \min_{\mathbf{k}, \{\mathbf{g}_i\}_{i=1}^C} & \sum_{i=1}^C \left(\frac{1}{2} \|\mathbf{f}_i * \mathbf{y} - \mathbf{k} * \mathbf{g}_i\|_2^2 + \lambda_i \|\mathbf{g}_i\|_1 \right) + \frac{\epsilon}{2} \|\mathbf{k}\|_2^2, \\ \text{subject to } & \|\mathbf{k}\|_1 = 1, \quad \mathbf{k} \geq 0. \end{aligned} \quad (5)$$

B. Efficient Minimization via Half-quadratic Splitting

Problem (5) is non-smooth so that traditional gradient-based optimization algorithms cannot be considered. Moreover, to facilitate the subsequent unrolling procedure, the algorithm needs to be simple (to simplify the network structure) and converge quickly (to reduce the number of layers required). Based on these concerns, we adopt the half-quadratic splitting algorithm [55]. This algorithm is simple but effective, and has been successfully employed in many previous deblurring techniques [56], [13], [16].

The basic idea is to perform variable-splitting and then alternating minimization on the penalty function. To this end, we first cast (5) into the following approximation model:

$$\begin{aligned} \min_{\mathbf{k}, \{\mathbf{g}_i, \mathbf{z}_i\}_{i=1}^C} & \sum_{i=1}^C \left(\frac{1}{2} \|\mathbf{f}_i * \mathbf{y} - \mathbf{k} * \mathbf{g}_i\|_2^2 \right. \\ & \left. + \lambda_i \|\mathbf{z}_i\|_1 + \frac{1}{2\zeta_i} \|\mathbf{g}_i - \mathbf{z}_i\|_2^2 \right) + \frac{\epsilon}{2} \|\mathbf{k}\|_2^2, \\ \text{subject to } & \|\mathbf{k}\|_1 = 1, \quad \mathbf{k} \geq 0, \end{aligned} \quad (6)$$

by introducing auxiliary variables $\{\mathbf{z}_i\}_{i=1}^C$, where $\zeta_i, i = 1, \dots, C$ are regularization parameters. It is well known that as $\zeta_i \rightarrow 0$ the sequence of solutions to (6) converges to that of (5) [57]. In a similar manner to [13], we then alternately minimize over $\{\mathbf{g}_i\}_{i=1}^C, \{\mathbf{z}_i\}_{i=1}^C$ and \mathbf{k} and iterate until convergence². Specifically, at the l -th iteration, we execute the following minimizations sequentially:

$$\begin{aligned} \mathbf{g}_i^{l+1} & \leftarrow \arg \min_{\mathbf{g}_i} \frac{1}{2} \|\mathbf{f}_i * \mathbf{y} - \mathbf{k}^l * \mathbf{g}_i\|_2^2 + \frac{1}{2\zeta_i} \|\mathbf{g}_i - \mathbf{z}_i^l\|_2^2, \quad \forall i, \\ \mathbf{z}_i^{l+1} & \leftarrow \arg \min_{\mathbf{z}_i} \frac{1}{2\zeta_i} \|\mathbf{g}_i^{l+1} - \mathbf{z}_i\|_2^2 + \lambda_i \|\mathbf{z}_i\|_1, \quad \forall i, \\ \mathbf{k}^{l+1} & \leftarrow \arg \min_{\mathbf{k}} \sum_{i=1}^C \frac{1}{2} \|\mathbf{f}_i * \mathbf{y} - \mathbf{k} * \mathbf{g}_i^{l+1}\|_2^2 + \frac{\epsilon}{2} \|\mathbf{k}\|_2^2, \\ \text{subject to } & \|\mathbf{k}\|_1 = 1, \quad \mathbf{k} \geq 0. \end{aligned} \quad (7)$$

For notational brevity, we will consistently use i to index the filters and l to index the layers (iteration) henceforth. The notations $\{\cdot\}_i$ and $\{\cdot\}_l$ collects every filter and layer components, respectively. As it is, problem (5) is non-convex over the joint variables \mathbf{k} and $\{\mathbf{g}_i\}_i$ and proper initialization is crucial to get good solutions. However, it is difficult to find appropriate initializations that perform well under various practical scenarios. An alternative strategy that has been commonly employed is to use different parameters per iteration [55], [11], [23], [13]. For example, λ_i 's are typically chosen as a large value from the beginning, and then gradually decreased towards a small constant. In [55] the values of ζ_i 's decrease as the algorithm proceeds for faster convergence. In numerical analysis and optimization, this strategy is called the continuation method and its effectiveness is known for solving non-convex problems [58]. By adopting this strategy, we choose different parameters $\{\zeta_i^l, \lambda_i^l\}_{i,l}$ across the iterations. We take this idea one step further by optimizing the filters across

²In the non-blind deconvolution literature, a formal convergence proof has been shown in [55], while for blind deconvolution, empirical convergence has been frequently observed as shown in [11], [13], etc.

iterations as well, i.e. we design filters $\{\mathbf{f}_i^l\}_{i,l}$. Consequently, the alternating minimization scheme in (7) becomes:

$$\mathbf{g}_i^{l+1} \leftarrow \arg \min_{\mathbf{g}_i} \frac{1}{2} \|\mathbf{f}_i^l * \mathbf{y} - \mathbf{k}^l * \mathbf{g}_i\|_2^2 + \frac{1}{2\zeta_i^l} \|\mathbf{g}_i - \mathbf{z}_i^l\|_2^2, \quad \forall i, \quad (8)$$

$$\mathbf{z}_i^{l+1} \leftarrow \arg \min_{\mathbf{z}_i} \frac{1}{2\zeta_i^l} \|\mathbf{g}_i^{l+1} - \mathbf{z}_i\|_2^2 + \lambda_i^l \|\mathbf{z}_i\|_1, \quad \forall i, \quad (9)$$

$$\mathbf{k}^{l+1} \leftarrow \arg \min_{\mathbf{k}} \sum_{i=1}^C \frac{1}{2} \|\mathbf{f}_i^l * \mathbf{y} - \mathbf{k} * \mathbf{g}_i^{l+1}\|_2^2 + \frac{\epsilon}{2} \|\mathbf{k}\|_2^2, \quad (10)$$

subject to $\|\mathbf{k}\|_1 = 1, \quad \mathbf{k} \geq 0$.

We summarize the complete algorithm in Algorithm 1, where δ in Step 1 is the impulse function. Problem (8) can be efficiently solved by making use of the Discrete Fourier Transform (DFT) and its solution is given in Step 5 of Algorithm 1, where $*$ is the complex conjugation and \odot is the Hadamard (elementwise) product operator. The operations are to be interpreted elementwise when acting on matrices and vectors. We let $\widehat{\cdot}$ denote the DFT and \mathcal{F}^{-1} be the inverse DFT. The closed-form solution to problem (9) is well known and can be found in Step 6, where, $\mathcal{S}_\lambda(\cdot)$ is the soft-thresholding operator defined as:

$$\mathcal{S}_\lambda(x) = \text{sgn}(x) \cdot \max\{|x| - \lambda, 0\}.$$

Subproblem (10) is a quadratic programming problem with a simplex constraint. While in principle, it may be solved using iterative numerical algorithms, in the blind deblurring literature an approximation scheme is often adopted. The unconstrained quadratic programming problem is solved first (again using DFT) to obtain a solution; its negative coefficients are then thresholded out, and finally normalized to have unit sum (Steps 8–10 of Algorithm 1). We define $[x]_+ = \max\{x, 0\}$. This function is commonly called the Rectified Linear Unit (ReLU) in neural network terminology [59]. Note that in Step 9 of Algorithm 1, we are adopting a common practice [8], [16] by thresholding the kernel coefficients using a positive constant (which is usually set as a constant parameter multiplying the maximum of the kernel coefficients); to avoid the non-smoothness of the maximum operation, we use the log-sum-exp function as a smooth surrogate.

We note that the quality of the outputs and the convergence speed depend crucially on the filters $\{\mathbf{f}_i^l\}_{i,l}$ and parameters $\{\zeta_i^l, \lambda_i^l\}_{i,l}$, which are difficult to infer due to the huge variety of real world data. Under traditional settings, they are usually determined by hand crafting or domain knowledge. For example, in [23], [16] $\{\mathbf{f}_i^l\}_{i,l}$ are taken as Prewitt filters while $\{\lambda_i^l\}_l$'s are chosen as geometric sequences. Their optimal values thus remain unclear. To optimize the performance, we learn (adapt) the filters and parameters by using training images in a deep learning set-up via back-propagation. A detailed visual comparison between filters commonly used in conventional algorithms and filters learned through real datasets by DUBLID is provided in Section IV-B.

Algorithm 1 Half-quadratic Splitting Algorithm for Blind Deblurring with Continuation

Input: Blurred image \mathbf{y} , filter banks $\{\mathbf{f}_i^l\}_{i,l}$, positive constant parameters $\{\zeta_i^l, \lambda_i^l\}_{i,l}$, number of iterations³ L and ϵ .
Output: Estimated kernel $\tilde{\mathbf{k}}$, estimated feature maps $\{\tilde{\mathbf{g}}_i\}_{i=1}^C$.

- 1: Initialize $\mathbf{k}^1 \leftarrow \delta; \mathbf{z}_i^1 \leftarrow 0, i = 1, \dots, C$.
 - 2: **for** $l = 1$ **to** L **do**
 - 3: **for** $i = 1$ **to** C **do**
 - 4: $\mathbf{y}_i^l \leftarrow \mathbf{f}_i^l * \mathbf{y}$,
 - 5: $\mathbf{g}_i^{l+1} \leftarrow \mathcal{F}^{-1} \left\{ \frac{\zeta_i^l \widehat{\mathbf{k}}^l * \odot \widehat{\mathbf{y}}_i^l + \widehat{\mathbf{z}}_i^l}{\zeta_i^l |\widehat{\mathbf{k}}^l|^2 + 1} \right\}$,
 - 6: $\mathbf{z}_i^{l+1} \leftarrow \mathcal{S}_{\lambda_i^l \zeta_i^l} \{\mathbf{g}_i^{l+1}\}$,
 - 7: **end for**
 - 8: $\mathbf{k}^{l+\frac{1}{3}} \leftarrow \mathcal{F}^{-1} \left\{ \frac{\sum_{i=1}^C \widehat{\mathbf{z}}_i^{l+1} * \odot \widehat{\mathbf{y}}_i^l}{\sum_{i=1}^C |\widehat{\mathbf{z}}_i^{l+1}|^2 + \epsilon} \right\}$,
 - 9: $\mathbf{k}^{l+\frac{2}{3}} \leftarrow \left[\mathbf{k}^{l+\frac{1}{3}} - \beta^l \log \left(\sum_i \exp \left(\mathbf{k}_i^{l+\frac{1}{3}} \right) \right) \right]_+$,
 - 10: $\mathbf{k}^{l+1} \leftarrow \frac{\mathbf{k}^{l+\frac{2}{3}}}{\|\mathbf{k}^{l+\frac{2}{3}}\|_1}$,
 - 11: $l \leftarrow l + 1$.
 - 12: **end for**
-

After Algorithm 1 converges, we obtain the estimated feature maps $\{\tilde{\mathbf{g}}_i\}_i$ and the estimated kernel $\tilde{\mathbf{k}}$. Because of the low-pass nature of $\tilde{\mathbf{k}}$, using it alone is inadequate to reliably recover the sharp image \mathbf{x} and regularization is needed. We may infer from (4) that, as $\tilde{\mathbf{k}}$ approximates \mathbf{k} , $\tilde{\mathbf{g}}_i$ should approximate $\mathbf{f}_i * \mathbf{x}$. Therefore, we retrieve \mathbf{x} by solving the following optimization problem:

$$\begin{aligned} \tilde{\mathbf{x}} &\leftarrow \arg \min_{\mathbf{x}} \frac{1}{2} \|\mathbf{y} - \tilde{\mathbf{k}} * \mathbf{x}\|_2^2 + \sum_{i=1}^C \frac{\eta_i}{2} \|\mathbf{f}_i^L * \mathbf{x} - \tilde{\mathbf{g}}_i\|_2^2 \\ &= \mathcal{F}^{-1} \left\{ \frac{\widehat{\tilde{\mathbf{k}}} * \widehat{\mathbf{y}} + \sum_{i=1}^C \eta_i \widehat{\mathbf{f}}_i^L * \odot \widehat{\tilde{\mathbf{g}}}_i}{|\widehat{\tilde{\mathbf{k}}}|^2 + \sum_{i=1}^C \eta_i |\widehat{\mathbf{f}}_i^L|^2} \right\}, \end{aligned} \quad (11)$$

where η_i 's are positive regularization parameters.

III. ALGORITHM UNROLLING FOR DEEP BLIND IMAGE DEBLURRING (DUBLID)

A. Network Construction via Algorithm Unrolling

Each step of Algorithm 1 is in analytic form and can be implemented using a series of basic functional operations. In particular, step 5 and step 8 in Algorithm 1 can be implemented according to the diagrams in Fig. 1a and Fig. 1b, respectively. The soft-thresholding operation in step 6 may be implemented using two ReLU operations by recognizing that $\mathcal{S}_\lambda(x) = [x - \lambda]_+ - [-x - \lambda]_+$. Similarly, (11) may be implemented according to Fig. 1c. Therefore, each iteration of

³ L refers to the number of outer iterations, which subsequently becomes the number of network layers in Section III-A. While in traditional iterative algorithms it is commonly determined by certain termination criteria, this approach is difficult to implement for neural networks. Therefore, in this work we choose it through cross-validation as is done in [30], [32].

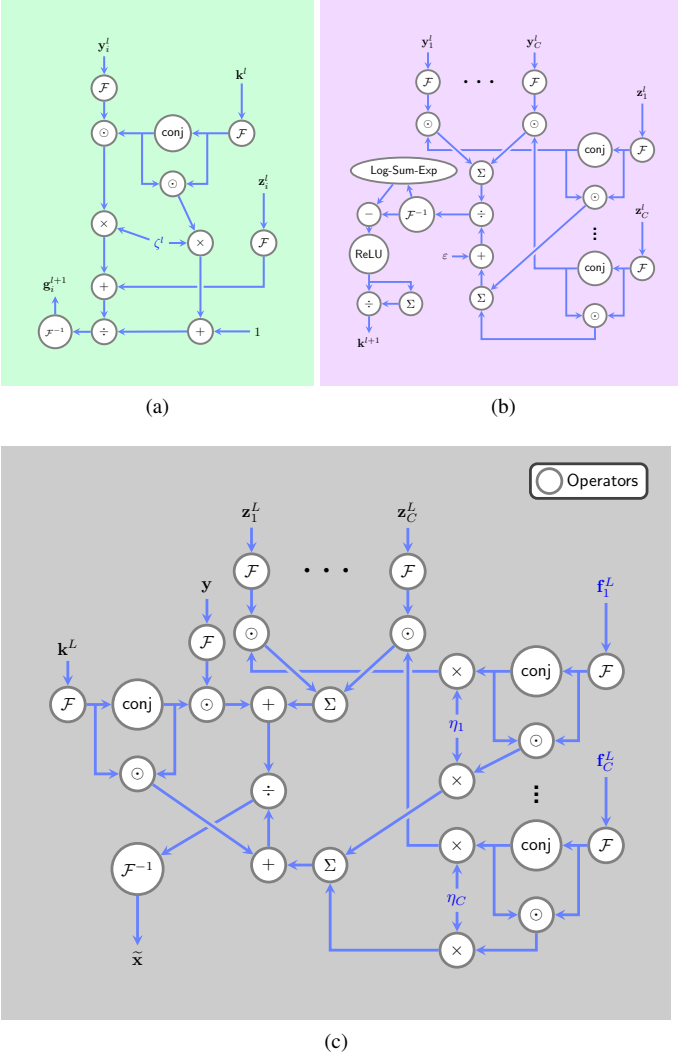


Fig. 1. Block diagram representations of (a) step 5 in Algorithm 1, (b) step 8 in Algorithm 1 and (c) Equation (11). After unrolling the iterative algorithm to form a multi-layer network, the diagrammatic representations serve as building blocks that repeat themselves from layer to layer. The parameters (ζ and η) are learned from real datasets and colored in blue.

Algorithm 1 admits a diagram representation, and repeating it L times yields an L -layer neural network (as shown in Fig. 2) which corresponds to executing Algorithm 1 with L iterations. For notational brevity, we concatenate the parameters in each layer and let $\mathbf{f}^l = (\mathbf{f}_i^l)_{i=1}^C$, $\zeta^l = (\zeta_i^l)_{i=1}^C$, $\lambda^l = (\lambda_i^l)_{i=1}^C$ and $\eta = (\eta_i)_{i=1}^C$. We also concatenate \mathbf{y}_i^l 's, \mathbf{z}_i^l 's and \mathbf{g}_i^l 's by letting $\mathbf{y}^l = (\mathbf{y}_i^l)_{i=1}^C$, $\mathbf{z}^l = (\mathbf{z}_i^l)_{i=1}^C$ and $\mathbf{g}^l = (\mathbf{g}_i^l)_{i=1}^C$, respectively.

When the blur kernel has a large size (which may happen due to fast motion), it is desirable to alter the spatial size of the filter banks $\{\mathbf{f}_i\}_i$ in different layers. In blind deblurring, kernel recovery is frequently performed stage-wise in a coarse-to-fine scheme: the kernel is initially estimated from a high-level summary of the image features, and then progressively refined by introducing lower-level details. For example, in [9] an initial kernel is obtained by masking out detrimental gradients, followed by iterative refinements. Other works [8], [23], [16] use a multi-scale pyramid implementation by decomposing the images into a Gaussian pyramid and progressively refine

the kernel in each scale. We may integrate this scheme into Algorithm 1 by choosing large filters in early iterations, so that they are capable of capturing rather high-level features, and gradually decrease their size to let fine details emerge. Translating this into the network, we may expect the following relationship among the sizes of kernels in different layers:

$$\text{size of } \mathbf{f}_i^1 \geq \text{size of } \mathbf{f}_i^2 \geq \text{size of } \mathbf{f}_i^3 \geq \dots$$

In practice, large filters may be difficult to train due to the large number of parameters they contain. To address this issue, we produce large filters by cascading small 3×3 filters, following the same principle as [60]. Formally, we set $\mathbf{f}_i^L = \mathbf{w}_{i1}^L$ where $\{\mathbf{w}_{i1}^L\}_{i=1}^C$ is a collection of 3×3 filters, and recursively obtain \mathbf{f}_i^l by filtering \mathbf{f}_i^{l+1} through 3×3 filters $\{\mathbf{w}_{ij}^l\}_{i,j=1}^C$:

$$\mathbf{f}_i^l \leftarrow \sum_{j=1}^C \mathbf{w}_{ij}^l * \mathbf{f}_j^{l+1}, \quad i = 1, 2, \dots, C.$$

Embedding the above into the network, we obtain the structure depicted in Fig. 3. Note that \mathbf{y}^l can now be obtained more efficiently by filtering \mathbf{y}^{l+1} through \mathbf{w}^l . Also note that $\{\mathbf{w}_{ij}^l\}_{i,j=1}^C$ are to be learned as marked in Fig. 3. Experimental justification of cascaded filtering is provided in Fig. 5.

B. Training

In a given training set, for each blurred image $\mathbf{y}_t^{\text{train}} (t = 1, \dots, T)$, we let the corresponding sharp image and kernel be $\mathbf{x}_t^{\text{train}}$ and $\mathbf{k}_t^{\text{train}}$, respectively. We do not train the parameter ε in step 8 of Algorithm 1 because it simply serves as a small constant to avoid division by zeros. We re-parametrize ζ_i^l in step 6 of Algorithm 1 by letting $b_i^l = \lambda_i^l \zeta_i^l$ and denote $b^l = (b_i^l)_{i=1}^C, l = 1, \dots, L$. The network outputs $\tilde{\mathbf{x}}_t, \tilde{\mathbf{k}}_t$ corresponding to $\mathbf{y}_t^{\text{train}}$ depend on the parameters $\mathbf{w}^l, b^l, \zeta^l, \beta^l, l = 1, 2, \dots, L$. In addition, $\tilde{\mathbf{x}}_t$ depends on η . We train the network to determine these parameters by solving the following optimization problem:

$$\min_{\{\mathbf{w}^l, b^l, \zeta^l, \beta^l\}_l, \eta, \{\tau_t\}_t} \sum_{t=1}^T \frac{\kappa_t}{2} \text{MSE} \left(\tilde{\mathbf{k}}_t (\{\mathbf{w}^l, b^l, \zeta^l, \beta^l\}_l), \mathcal{T}_{\tau_t} \{\mathbf{k}_t^{\text{train}}\} \right) + \frac{1}{2} \text{MSE} \left(\tilde{\mathbf{x}}_t (\{\mathbf{w}^l, b^l, \zeta^l, \beta^l\}_l, \eta), \mathcal{T}_{-\tau_t} \{\mathbf{x}_t^{\text{train}}\} \right)$$

$$\text{subject to } b_i^l \geq 0, \lambda_i^l \geq 0, \beta^l \geq 0, \quad l = 1, \dots, L, i = 1, \dots, C, \quad (12)$$

where $\kappa_t > 0$ is a constant parameter which is fixed to $\frac{\kappa_0}{\max_i |(\mathbf{k}_i^{\text{train}})_i|^2}$, and we determined $\kappa_0 = 10^5$ through cross-validation. $\text{MSE}(\cdot, \cdot)$ is the (empirical) Mean-Square-Error loss function, and $\mathcal{T}_\tau \{\cdot\}$ is the translation operator in 2D that performs a shift by $\tau \in \mathbb{R}^2$. The shift operation is used here to compensate for the inherent shifting ambiguity in blind deconvolution [23].

In the training process, when working on each mini-batch, we alternate between minimizing over $\{\tau_t\}_t$ and performing a projected stochastic gradient descent step. Specifically, we first determine the optimal $\{\tau_t\}_t$ efficiently via a grid search in the Fourier domain. We then take one stochastic gradient descent step; the analytic derivation of the gradient is included in Appendix A. Finally, we threshold out the negative coefficients of $\{b_i^l, \zeta_i^l, \beta^l\}_{i,l}$ to enforce the non-negativity constraints. We

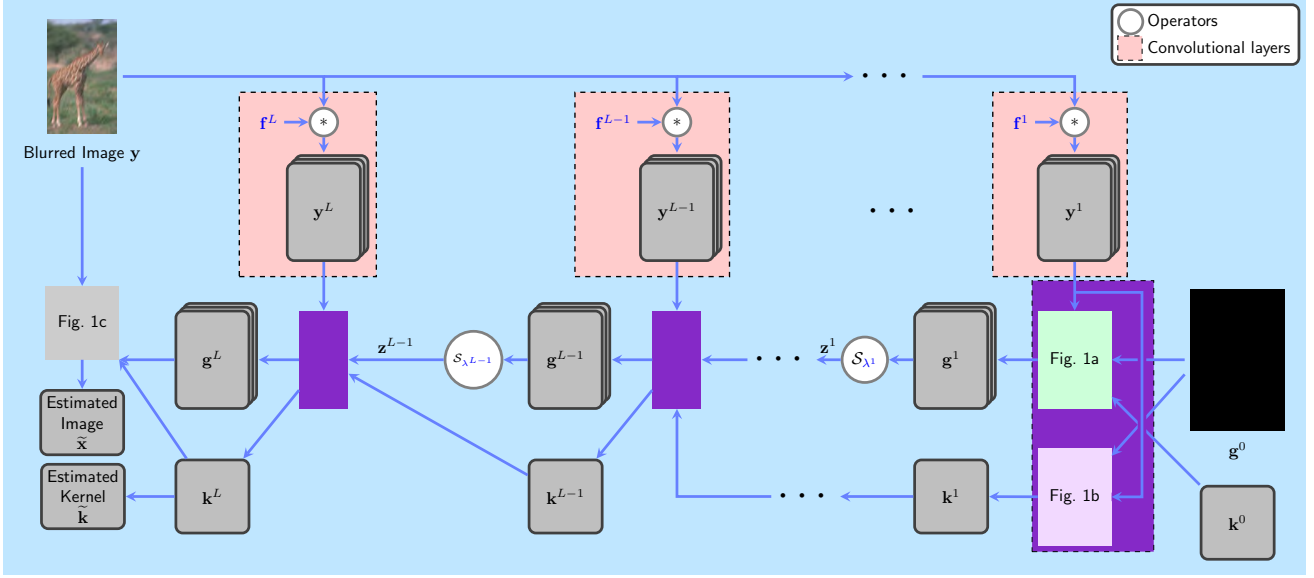


Fig. 2. Algorithm 1 unrolled as a neural network. The parameters that are learned from real datasets are colored in blue.

use the Adam algorithm [61] to accelerate the training speed. The learning rate is set to 1×10^{-3} initially and decayed by a factor of 0.5 every 20 epochs. We terminate training after 160 epochs. The parameters $\{b_i^l\}_{i,l}$ are initialized to 0.02, $\{c_i^l\}_{i,l}$ initialized to 1, $\{\beta^l\}_l$ initialized to 0, and $\{\eta_i\}_i$ initialized to 20, respectively. These values are again determined through cross-validation. The upper part (feature extraction portion) of the network in Fig. 3 resembles a CNN with linear activations (identities) and thus we initialize the weights according to [62].

C. Handling Color Images

For color images, the red, green and blue channels $y_r, y_g,$ and y_b are blurred by the same kernel, and thus the following model holds instead of (1):

$$y_c = \mathbf{k} * \mathbf{x}_c + \mathbf{n}_c, \quad c \in \{r, g, b\}.$$

To be consistent with existing literature, we modify \mathbf{w}^L in Fig. 3 to allow for multi-channel inputs. More specifically, \mathbf{y}^L is produced by the following formula:

$$\mathbf{y}_i^L = \sum_{c \in \{r, g, b\}} \mathbf{w}_{ic}^L * \mathbf{y}_c, \quad i = 1, \dots, C.$$

It is easy to check that, with \mathbf{w}^L and \mathbf{y}^L being replaced, all the components of the network can be left unchanged except for the module in Fig. 1c. This is because (4) no longer holds and is modified to the following:

$$\sum_{c \in \{r, g, b\}} \mathbf{w}_{ic} * \mathbf{y}_c = \mathbf{k} * \left(\sum_{c \in \{r, g, b\}} \mathbf{w}_{ic} * \mathbf{x}_c \right) + \mathbf{n}'_i, \quad i = 1, \dots, C,$$

where $\mathbf{n}'_i = \sum_{c \in \{r, g, b\}} \mathbf{w}_{ic} * \mathbf{n}$ represents Gaussian noise.

Problem (11) then becomes:

$$\begin{aligned} \{\widetilde{\mathbf{x}}_r, \widetilde{\mathbf{x}}_g, \widetilde{\mathbf{x}}_b\} \leftarrow \arg \min_{\mathbf{x}_r, \mathbf{x}_g, \mathbf{x}_b} \sum_{c \in \{r, g, b\}} \frac{1}{2} \left\| \mathbf{y}_c - \widetilde{\mathbf{k}} * \mathbf{x}_c \right\|_2^2 \\ + \sum_{i=1}^C \frac{\eta_i}{2} \left\| \sum_{c \in \{r, g, b\}} \mathbf{w}_{ic} * \mathbf{x}_c - \widetilde{\mathbf{g}}_i \right\|_2^2, \end{aligned}$$

whose solution is given as follows:

$$\begin{aligned} \widetilde{\mathbf{x}}_r &= \mathcal{F}^{-1} \left\{ \frac{\mathbf{m}_{rr} \odot \mathbf{b}_r + \mathbf{m}_{rg} \odot \mathbf{b}_g + \mathbf{m}_{rb} \odot \mathbf{b}_b}{\mathbf{d}} \right\}, \\ \widetilde{\mathbf{x}}_g &= \mathcal{F}^{-1} \left\{ \frac{\mathbf{m}_{rg}^* \odot \mathbf{b}_r + \mathbf{m}_{gg} \odot \mathbf{b}_g + \mathbf{m}_{gb} \odot \mathbf{b}_b}{\mathbf{d}} \right\}, \\ \widetilde{\mathbf{x}}_b &= \mathcal{F}^{-1} \left\{ \frac{\mathbf{m}_{rb}^* \odot \mathbf{b}_r + \mathbf{m}_{gb}^* \odot \mathbf{b}_g + \mathbf{m}_{bb} \odot \mathbf{b}_b}{\mathbf{d}} \right\}, \end{aligned}$$

where

$$\begin{aligned} \mathbf{m}_{rr} &= \mathbf{c}_{gg} \odot \mathbf{c}_{bb} - |\mathbf{c}_{gb}|^2, \quad \mathbf{m}_{rg} = \mathbf{c}_{rb} \odot \mathbf{c}_{gb}^* - \mathbf{c}_{bb} \odot \mathbf{c}_{rg}, \\ \mathbf{m}_{rb} &= \mathbf{c}_{rg} \odot \mathbf{c}_{gb} - \mathbf{c}_{gg} \odot \mathbf{c}_{rb}, \quad \mathbf{m}_{gg} = \mathbf{c}_{bb} \odot \mathbf{c}_{rr} - |\mathbf{c}_{rb}|^2, \\ \mathbf{m}_{gb} &= \mathbf{c}_{rg}^* \odot \mathbf{c}_{rb} - \mathbf{c}_{rr} \odot \mathbf{c}_{gb}, \quad \mathbf{m}_{bb} = \mathbf{c}_{rr} \odot \mathbf{c}_{gg} - |\mathbf{c}_{rg}|^2. \end{aligned}$$

Here,

$$\begin{aligned} \mathbf{c}_{cc'} &= \sum_{i=1}^C \eta_i \widehat{\mathbf{w}}_{ic}^* \odot \widehat{\mathbf{w}}_{ic'} + |\widehat{\mathbf{k}}|^2 \delta_{cc'}, \quad c, c' \in \{r, g, b\}, \\ \mathbf{b}_c &= \widehat{\mathbf{k}}^* \odot \widehat{\mathbf{y}}_c + \sum_{i=1}^C \eta_i \widehat{\mathbf{w}}_{ic}^* \odot \widehat{\mathbf{g}}_i, \quad c \in \{r, g, b\}, \\ \mathbf{d} &= \left(\mathbf{c}_{gg} \odot \mathbf{c}_{rr} - |\mathbf{c}_{rg}|^2 \right) \odot \mathbf{c}_{bb} + 2\Re\{\mathbf{c}_{rb}^* \odot \mathbf{c}_{rg} \odot \mathbf{c}_{gb}\} \\ &\quad - |\mathbf{c}_{gb}|^2 \odot \mathbf{c}_{rr} - |\mathbf{c}_{rb}|^2 \odot \mathbf{c}_{gg}, \end{aligned}$$

and $\delta_{cc'}$ is the Kronecker delta function. These analytical formulas may be represented using diagrams similar to Fig. 1c and embedded into a network.

IV. EXPERIMENTAL VERIFICATION

A. Experimental Setups

1) Datasets, Training and Test Setup:

- **Training for linear kernels:** For the images we used the Berkeley Segmentation Data Set 500 (BSDS500) [63] which is a large dataset of 500 natural images that is explicitly divided into disjoint training, validation and test subsets. Here we use 300 images for training by combining the training and validation images.

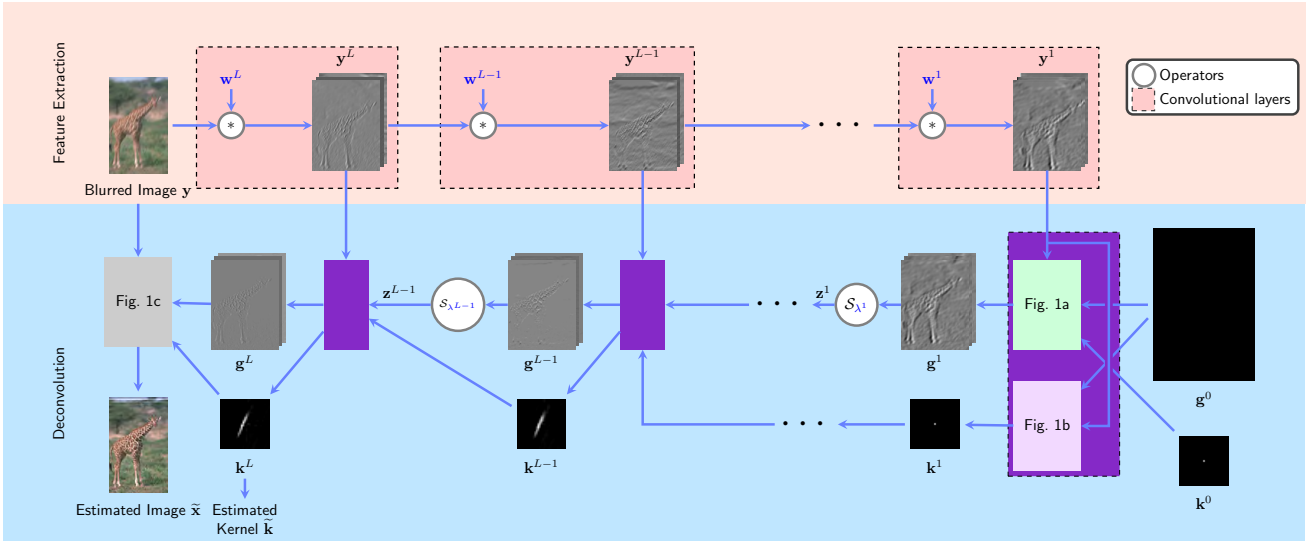


Fig. 3. DUBLID: using a cascade of small 3×3 filters instead of large filters (as compared to the network in Fig. 2) reduces the dimensionality of the parameter space, and the network can be easier to train. Intermediate data (hidden layers) on the trained network are also shown. It can be observed that, as l increases, g^l and y^l evolve in a coarse-to-fine manner. The parameters that will be learned from real datasets are colored in blue.

We generated 256 linear kernels by varying the length and angle of the kernels (refer to Section IV-C for details).

- **Training for nonlinear kernels:** We used the Microsoft COCO [64] dataset which is a large-scale object detection, segmentation, and captioning dataset containing 330K images.

Nonlinear kernels: We generated around 30,000 real world kernels by recording camera motion trajectories (refer to Sec. IV-D for details).

- **Testing for the linear kernel experiments:** We use 200 images from the test portion of BSDS500 as test images and we randomly choose four kernels of different angle and length as test kernels.
- **Testing for the nonlinear kernel experiments:** We test on *two* benchmark datasets specifically developed for evaluating blind deblurring with non-linear kernels: 1.) 4 images and 8 kernels by Levin *et al.* [22] and 2.) 80 images and 8 kernels from Sun *et al.* [12].

2) *Comparisons Against State of the Art Methods:* We compare against **five** methods:

- Perrone *et al.* [23] - a representative iterative blind image deblurring method based on total-variation minimization, which demonstrated state-of-the-art performance amongst traditional iterative methods. (TPAMI 2016)
- Chakrabarti *et al.* [28] - one of the first neural network blind image deblurring methods. (CVPR 2016)
- Nah *et al.* [40] - a recent deep learning method based on the state-of-the-art ResNet [65]. (CVPR 2017)
- Kupyn *et al.* [66] - a recent deep learning method based on the state-of-the-art generative adversarial networks (GAN) [67]. (CVPR 2018)
- Xu *et al.* [29] - a recent state of the art deep learning method focused on motion kernel estimation. (TIP 2018)

3) *Quantitative Performance Measures:* To quantitatively assess the performance of various methods in different scenarios, we use the following metrics:

- Peak-Signal-to-Noise Ratio (PSNR);

TABLE I
EFFECTS OF DIFFERENT VALUES OF LAYER L .

Number of layers	6	8	10	12
PSNR (dB)	26.55	26.94	27.30	27.35
RMSE ($\times 10^{-3}$)	1.96	2.06	1.67	1.66

- Improvement in Signal-to-Noise-Ratio (ISNR), which is given by $ISNR = 10 \log_{10} \left(\frac{\|y-x\|_2^2}{\|\tilde{x}-x\|_2^2} \right)$ where \tilde{x} is the reconstructed image;
- Structural Similarity Index (SSIM) [68];
- (Empirical) Root-Mean-Square Error (RMSE) computed between the estimated kernel and the ground truth kernel.

We note that for selected methods, RMSE numbers (against the ground truth kernel) are *not* reported in Tables III, IV and V because those methods directly estimate just the deblurred image (and not the blur kernel).

B. Ablation Study of the Network

To provide insights into the design of our network, we first carry out a series of experimental studies to investigate the influence of two key design variables: 1.) the number of layers L , and 2.) the number of filters C . We monitor the performance using PSNR and RMSE. The results in Tables I and II are for linear kernels with the same training-test configuration as in Section IV-A. The trends over L and C were found to be similar for non-linear kernels as well.

We first study the influence of different number of layers L . We alter L , i.e. the proposed DUBLID is learned as in Section III-B, each time as L is varied. Table I summarizes the numerical scores corresponding to different L . Clearly, the network performs better with increasing L , consistent with common observations [69], [65]. In addition, the network performance improves marginally after L reaches 10. We thus fix $L = 10$ subsequently. For all results in Table I, the number of filters C is fixed to 16.

TABLE II
EFFECTS OF DIFFERENT VALUES OF NUMBER OF FILTERS C .

Number of filters	8	16	32
PSNR (dB)	26.55	27.30	27.16
RMSE ($\times 10^{-3}$)	1.99	1.67	1.93

We next study the effects of different values of C in a similar fashion. The network performance over different choices of C is summarized in Table II. It can be seen that the network performance clearly improves as C increases from 8 to 16. However, the performance slightly drops when C increases further, presumably because of overfitting. We thus fix $C = 16$ henceforth.

To corroborate the network design choices made in Section III-A, we illustrate DUBLID performance for different filter choices. We first verify the significance of learning the filters $\{\mathbf{w}^l\}_l$ (and in turn $\{\mathbf{f}_i^l\}_{i,l}$) and compare the performance with a typical choice of analytical filters, the Sobel filters, in Fig. 4. Note that by employing Sobel filters, the network reduces to executing TV-based deblurring but for a small number of iterations, which coincides with the number of layers L . For fairness in comparison, the fixed Sobel filter version of DUBLID (called DUBLID-Sobel) is trained exactly as in Section III-B to optimize other parameters. As Fig. 4 reveals, DUBLID-Sobel is unable to accurately recover the kernel. Indeed, such phenomenon has been observed and analytically studied by Levin *et al.* [22], where they point out that traditional gradient-based approaches can easily get stuck at a delta solution. To gain further insight, we visualize the learned filters as well as the Sobel filters in Fig. 4a and Fig. 4b. The learned filters demonstrate richer variations than known analytic (Sobel) filters and are able to capture higher-level image features as l grows. This enables the DUBLID network to better recover the kernel coefficients subsequently. Quantitatively, the PSNR achieved by DUBLID-Sobel for $L = 10$ and $C = 16$ on the same training-test set up is 18.60 dB, which implies that DUBLID achieves a 8.7 dB gain by explicitly optimizing filters in a data-adaptive fashion.

Finally, we show the effectiveness of cascaded filtering. To this end, we compare with the alternative scheme of fixing the size of $\{\mathbf{f}_i^l\}_{i,l}$ by restricting $\{\mathbf{w}^l\}_l$ to be of size 1×1 whenever $l < L$. The results are shown in Fig. 5. By employing learnable filters, the network becomes capable of capturing the correct directions of blur kernels as shown in Fig. 5b. In the absence of cascaded filtering though, the recovered kernel is still coarse – a limitation that is overcome by using cascaded filtering, verified in Fig. 5c.

C. Evaluation on Linear Kernels

We use the training and validation portions of the BSDS500 [70], [63] dataset as training images. The linear motion kernels are generated by uniformly sampling 16 angles in $[0, \pi]$ and 16 lengths in $[5, 20]$, followed by 2D spatial interpolation. This gives a total number of 256 kernels. We then generate $T = 256 \times 300$ blurred images by convolving each kernel with each image and adding white Gaussian noise with standard deviation 0.01 (suppose the image intensity is

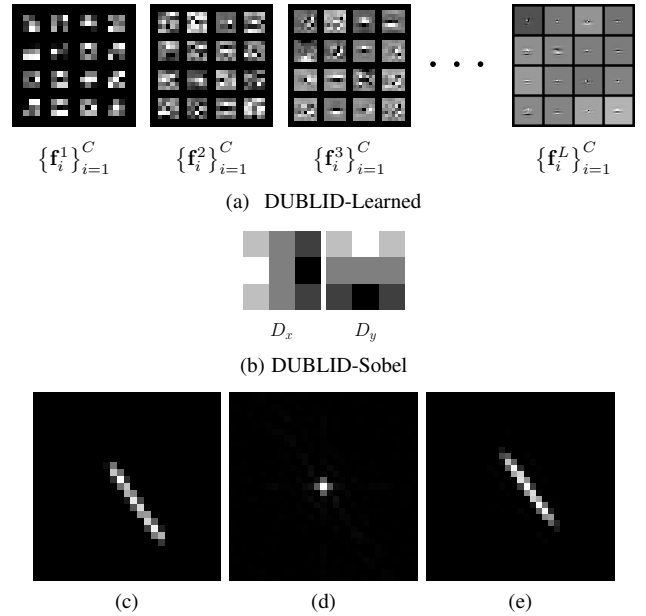


Fig. 4. Comparison of learned filters with analytic Sobel filters: (a) DUBLID learned filters. (b) Sobel filters that are commonly employed in traditional iterative blind deblurring algorithms. (c) An example motion blur kernel. (d) Reconstructed kernel using Sobel filters and (e) using learned filters.

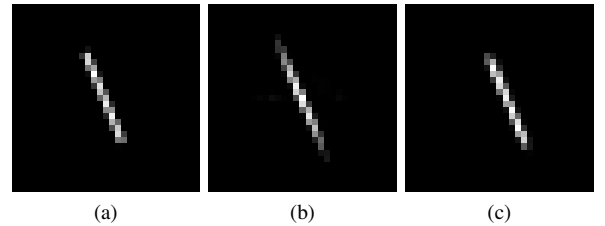


Fig. 5. The effectiveness of cascaded filtering: (a) a sample motion kernel. (b) Reconstructed kernel by fixing all \mathbf{f}_i^l 's to be of size 3×3 , which can be implemented by enforcing \mathbf{w}_{ij}^l to be of size 1×1 whenever $l < L$. (c) Reconstructed kernel using the cascaded filtering structure in Fig. 3.

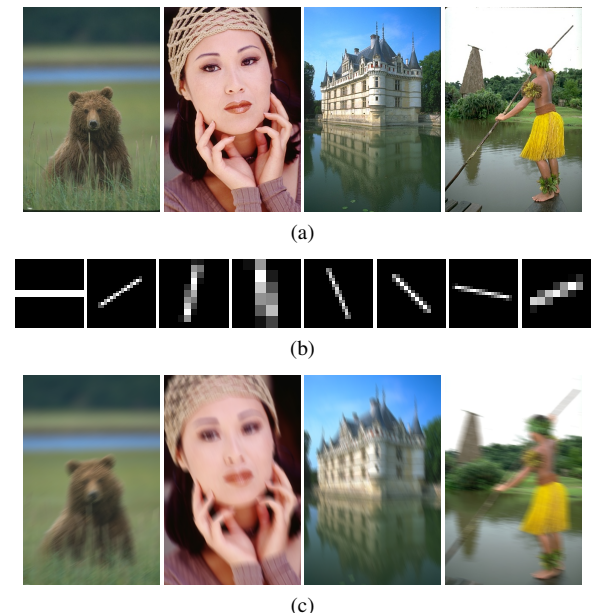


Fig. 6. Examples of images and kernels used for training. (a) The sharp images are collected from the BSDS500 dataset [70]. (b) The blur kernels are linear motion of different lengths and angles. (c) The blurred images are synthesized by convolving the sharp images with the blur kernels.

in range $[0, 1]$ individually. Examples of training samples (images and kernels) are shown in Fig. 6. We use 200 images from the test portion of the BSDS500 dataset [70] for evaluation. We randomly choose angles in $[0, \pi]$ and lengths in $[5, 20]$ to generate 4 test kernels. The images and kernels are convolved to synthesize 800 blurred images. White Gaussian noise (again with standard deviation 0.01) is also added.

Note that some of the state of the art methods compared against are only designed to recover the kernels, including [29] and [23]. To get the deblurred image, the non-blind method in [13] is used consistently. The scores are averaged and summarized in Table III. The RMSE values are computed over kernels, and smaller values indicate more accurate recoveries. For all other metrics on images, higher scores generally imply better performance. We do not include results from Chakrabarti *et al.* [28] here because that method works on grayscale images only. Table III confirms that DUBLID outperforms competing state-of-the art algorithms by a significant margin.

Fig. 7 shows four example images and kernels for a qualitative comparison. The two top-performing methods, Perrone *et al.* [23] and Nah *et al.* [40], are also included as representatives of iterative methods and deep learning methods, respectively. Although [23] can roughly infer the directions of the blur kernels, the recovered coefficients clearly differ from the groundtruth as evidenced by the spread-out branches. Consequently, destroyed local structures and false colors are clearly observed in the reconstructed images. Nah *et al.*'s method [40] does not suffer from false colors, yet the recovered images appear blurry. In contrast, DUBLID recovers kernels close to the groundtruth, and produces significantly fewer visually objectionable artifacts in the recovered images.

D. Evaluation on Non-linear Kernels

It has been observed in several previous works [22], [71] that realistic motion kernels often have non-linear shapes due to irregular camera motions, such as those shown in Fig. 8. Therefore, the capability to handle such kernels is crucial for a blind motion deblurring method.

We generate training kernels by interpolating the paths provided by [71] and those created by ourselves: specifically, we record the camera motion trajectories using the Vicon system, and then interpolate the trajectories spatially to create motion kernels. We further augment these kernels by scaling over 4 different scales and rotating over 8 directions. In this way, we build around 30,000 training kernels in total⁴. The blurred images for training are synthesized by randomly picking a kernel and convolving with it. Gaussian noise of standard deviation 0.01 is again added. We use the standard image set from [22] (comprising 4 images and 8 kernels) and from [12] (comprising 80 images and 8 kernels) as the test sets. The average scores for both datasets are presented in Table IV and Table V, respectively. In both datasets, DUBLID emerges overall as the best method. The method of Chakrabarti *et al.* [28] performs second best in Table V. In Table IV, Perrone *et al.* [23] and the recent deep learning method of Xu *et al.*

[29] perform comparably and mildly worse than DUBLID. DUBLID however achieves the deblurring at a significantly lower computational cost as verified in Section IV-E.

Visual examples are shown in Figs. 9 and 10 for qualitative comparisons. It can be clearly seen that DUBLID is capable of more faithfully recovering the kernels, and hence produces reconstructed images of higher visual quality. In particular, DUBLID preserves local details better as shown in the zoom boxes of Figs. 9 and 10 while providing sharper images than Nah *et al.* [40], Chakrabarti *et al.* [28] and Kupyn *et al.* [66]. Finally, DUBLID is free of visually objectionable artifacts observed in Perrone *et al.* [23] and Xu *et al.* [29].

E. Computational Comparisons Against State of the Art

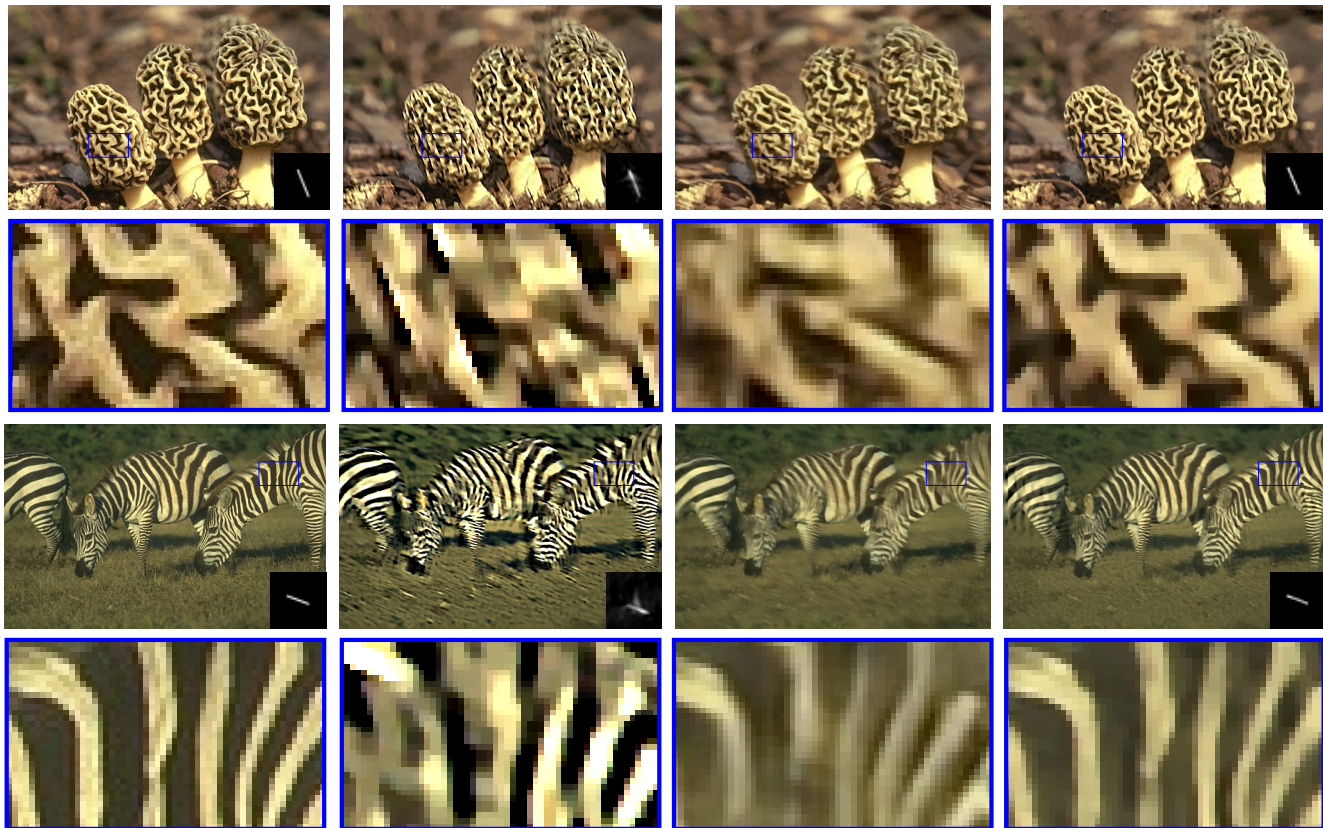
Table VI summarizes the execution (inference) times of each method for processing a typical blurred image of resolution 480×320 and a blur kernel of size 31×31 . The number of parameters for DUBLID is estimated as follows: for 3×3 filters w_{ij} , there are a total of $L = 10$ layers and in each layer there are $C^2 = 16 \times 16$ filters, which contribute to $3 \times 3 \times 16 \times 16 \times 10 \approx 2.3 \times 10^4$ parameters. Other parameters have negligible dimensions compared with w_{ij} and thus do not contribute significantly.

We include measurements of running time on both CPU and GPU. The – symbol indicates inapplicability. For instance, Chakrabarti *et al.* [28] and Nah *et al.* [40] only provide GPU implementations of their work and likewise Perrone *et al.*'s iterative method [23] is only implemented on a CPU. Specifically, the two benchmark platforms are: 1.) Intel Core i7-6900K, 3.20GHz CPU, 8GB of RAM, and 2.) an NVIDIA TITAN X GPU. The results in Table VI deliver two messages. First, the deep/neural network based methods are faster than their iterative algorithm counterparts, which is to be expected. Second, amongst the deep neural net methods DUBLID runs significantly faster than the others on both GPU and CPU, largely because it has significantly fewer parameters as seen in the final row of Table VI. Note that the number of parameters for competing deep learning methods are computed based on the description in their respective papers.

V. CONCLUSION

We propose an Algorithm Unrolling approach for Deep Blind image Deblurring (DUBLID). Our approach is based on recasting a generalized TV-regularized algorithm into a neural network, and optimizing its parameters via a custom designed backpropagation procedure. Unlike most existing neural network approaches, our technique has the benefit of interpretability, while sharing the performance benefits of modern neural network approaches. While some existing approaches excel for the case of linear kernels and others for non-linear, our method is versatile across a variety of scenarios and kernel choices – as is verified both visually and quantitatively. Further, DUBLID requires much fewer parameters leading to significant computational benefits over iterative methods as well as competing deep learning techniques.

⁴To re-emphasize, all learning based methods use the same training-test configuration for fairness in comparison.



(a) Groundtruth

(b) Perrone *et al.* [23](c) Nah *et al.* [40]

(d) DUBLID

Fig. 7. Qualitative comparisons on the BSDS500 [70] dataset. The blur kernels are placed at the right bottom corner. DUBLID recovers the kernel at higher accuracy and therefore the estimated images are more faithful to the groundtruth.

TABLE III
QUANTITATIVE COMPARISON OVER AN AVERAGE OF 200 IMAGES AND 4 KERNELS. THE BEST SCORES ARE IN BOLD FONTS.

Metrics	DUBLID	Perrone <i>et al.</i> [23]	Nah <i>et al.</i> [40]	Xu <i>et al.</i> [29]	Kupyn <i>et al.</i> [66]
PSNR (dB)	27.30	22.23	24.82	24.02	23.98
ISNR (dB)	4.45	2.06	1.92	1.12	1.05
SSIM	0.88	0.76	0.80	0.78	0.78
RMSE ($\times 10^{-3}$)	1.67	5.21	–	2.40	–

TABLE IV
QUANTITATIVE COMPARISON OVER AN AVERAGE OF 4 IMAGES AND 8 KERNELS FROM [22].

	DUBLID	Perrone <i>et al.</i> [23]	Nah <i>et al.</i> [40]	Chakrabarti <i>et al.</i> [28]	Xu <i>et al.</i> [29]	Kupyn <i>et al.</i> [66]
PSNR (dB)	27.15	26.79	24.51	23.21	26.75	23.98
ISNR (dB)	3.79	3.63	1.35	0.06	3.59	0.43
SSIM	0.89	0.89	0.81	0.81	0.89	0.80
RMSE ($\times 10^{-3}$)	3.87	3.83	–	4.33	3.98	–

TABLE V
QUANTITATIVE COMPARISON OVER AN AVERAGE OF 80 IMAGES AND 8 NONLINEAR MOTION KERNELS FROM [12].

	DUBLID	Perrone <i>et al.</i> [23]	Nah <i>et al.</i> [40]	Chakrabarti <i>et al.</i> [28]	Xu <i>et al.</i> [29]	Kupyn <i>et al.</i> [66]
PSNR (dB)	29.91	29.82	26.98	29.86	26.55	25.84
ISNR (dB)	4.11	4.02	0.86	4.06	0.43	0.15
SSIM	0.93	0.92	0.85	0.91	0.87	0.83
RMSE ($\times 10^{-3}$)	2.33	2.68	–	2.72	2.79	–

TABLE VI
RUNNING TIME COMPARISONS OVER DIFFERENT METHODS. THE IMAGE SIZE IS 480×320 AND THE KERNEL SIZE IS 31×31 .

	DUBLID	Chakrabarti <i>et al.</i> [28]	Nah <i>et al.</i> [40]	Perrone <i>et al.</i> [23]	Xu <i>et al.</i> [29]	Kupyn <i>et al.</i> [66]
CPU Time (s)	1.47	–	–	1462.90	6.89	10.29
GPU Time (s)	0.05	227.80	7.32	–	2.01	0.13
Number of Parameters	2.3×10^4	1.1×10^8	2.3×10^7	–	6.0×10^6	1.2×10^7



Fig. 8. Examples of realistic non-linear kernels [22].

APPENDIX A GRADIENTS COMPUTATION BY BACK-PROPAGATION

Here we develop the back-propagation rules for computing the gradients of DUBLID. We will use \mathbf{F} to denote the DFT operator and \mathbf{F}^* its adjoint operator, and $\mathbf{1}$ is a vector whose entries are all ones. \mathbf{I} refers to the identity matrix. The symbols $\mathcal{I}_{\{\cdot\}}$ means indicator vectors and $\text{diag}(\cdot)$ embeds the vector into a diagonal matrix. The operators $\mathbf{P}_{\mathbf{g}}$ and $\mathbf{P}_{\mathbf{k}}$ are projections that restrict the operand into the domain of the image and the kernel, respectively. Let \mathcal{L} be the cost function defined in (12). We derive its gradients w.r.t. its variables using the chain rule as follows:

$$\begin{aligned}\nabla_{\mathbf{w}_i^l} \mathcal{L} &= \nabla_{\mathbf{w}_i^l} \mathbf{y}_i^l \nabla_{\mathbf{y}_i^l} \mathcal{L} = \mathbf{R}_{\mathbf{w}_i^l} \mathbf{F} \text{diag}(\widehat{\mathbf{y}_i^{l+1}}) \mathbf{F}^* \nabla_{\mathbf{y}_i^l} \mathcal{L}, \\ \nabla_{\zeta_i^l} \mathcal{L} &= \nabla_{\zeta_i^l} \mathbf{z}_i^{l+1} \nabla_{\mathbf{z}_i^{l+1}} \mathcal{L} \\ &= \left[\frac{\widehat{\mathbf{k}}^{l*} \odot (\widehat{\mathbf{k}}^l \odot \widehat{\mathbf{g}}_i^l - \widehat{\mathbf{y}}_i^l)}{(|\widehat{\mathbf{k}}^l|^2 + \zeta_i^l)^2} \right]^T \mathbf{F}^* \left(\mathcal{I}_{\{|\mathbf{P}_{\mathbf{g}} \mathbf{g}_i^{l+1}| > b_i^l\}} \odot \nabla_{\mathbf{z}_i^{l+1}} \mathcal{L} \right),\end{aligned}$$

$$\nabla_{b_i^l} \mathcal{L} = \nabla_{b_i^l} \mathbf{z}_i^{l+1} \nabla_{\mathbf{z}_i^{l+1}} \mathcal{L} = \left(\mathcal{I}_{\{\mathbf{g}_i^{l+1} < -b_i^l\}} - \mathcal{I}_{\{\mathbf{g}_i^{l+1} > b_i^l\}} \right)^T \nabla_{\mathbf{z}_i^{l+1}} \mathcal{L},$$

where $\mathbf{R}_{\mathbf{w}_i^l}$ is the operator that extracts the components lying in the support of \mathbf{w}_i^l . Again using the chain rule,

$$\begin{aligned}\frac{\partial \mathcal{L}}{\partial \mathbf{k}^l} &= \frac{\partial \mathcal{L}}{\partial \mathbf{z}_i^{l+1}} \frac{\partial \mathbf{z}_i^{l+1}}{\partial \mathbf{k}^l}, \quad \frac{\partial \mathcal{L}}{\partial \mathbf{z}_i^l} = \frac{\partial \mathcal{L}}{\mathbf{z}_i^{l+1}} \frac{\partial \mathbf{z}_i^{l+1}}{\partial \mathbf{z}_i^l} + \frac{\partial \mathcal{L}}{\partial \mathbf{k}^l} \frac{\partial \mathbf{k}^l}{\partial \mathbf{z}_i^l}, \\ \frac{\partial \mathcal{L}}{\partial \mathbf{y}_i^l} &= \frac{\partial \mathcal{L}}{\mathbf{z}_i^{l+1}} \frac{\partial \mathbf{z}_i^{l+1}}{\partial \mathbf{y}_i^l} + \frac{\partial \mathcal{L}}{\partial \mathbf{k}^{l+1}} \frac{\partial \mathbf{k}^{l+1}}{\partial \mathbf{y}_i^l} + \frac{\partial \mathcal{L}}{\partial \mathbf{y}_i^{l-1}} \frac{\partial \mathbf{y}_i^{l-1}}{\partial \mathbf{y}_i^l}.\end{aligned}\quad (13)$$

We next derive each individual term in (13) as follows:

$$\begin{aligned}\frac{\partial \mathbf{z}_i^{l+1}}{\partial \widehat{\mathbf{g}}_i^{l+1}} &= \frac{\partial \mathbf{z}_i^{l+1}}{\mathbf{g}_i^{l+1}} \frac{\partial \mathbf{g}_i^{l+1}}{\widehat{\mathbf{g}}_i^{l+1}} = \text{diag} \left(\mathcal{I}_{\{|\mathbf{P}_{\mathbf{g}} \mathbf{g}_i^{l+1}| > b_i^l\}} \right) \mathbf{F}^*, \\ \frac{\partial \mathbf{z}_i^{l+1}}{\partial \mathbf{z}_i^l} &= \frac{\partial \mathbf{z}_i^{l+1}}{\widehat{\mathbf{g}}_i^{l+1}} \frac{\partial \widehat{\mathbf{g}}_i^{l+1}}{\widehat{\mathbf{z}}_i^l} \frac{\partial \widehat{\mathbf{z}}_i^l}{\partial \mathbf{z}_i^l}\end{aligned}\quad (14)$$

$$= \text{diag} \left(\mathcal{I}_{\{|\mathbf{P}_{\mathbf{g}} \mathbf{g}_i^{l+1}| > b_i^l\}} \right) \mathbf{F}^* \text{diag} \left(\frac{\zeta_i^l}{|\widehat{\mathbf{k}}^l|^2 + \zeta_i^l} \right) \mathbf{F},$$

$$\frac{\partial \mathbf{z}_i^{l+1}}{\partial \mathbf{y}_i^l} = \frac{\partial \mathbf{z}_i^{l+1}}{\widehat{\mathbf{g}}_i^{l+1}} \frac{\partial \widehat{\mathbf{g}}_i^{l+1}}{\partial \widehat{\mathbf{y}}_i^l} \frac{\partial \widehat{\mathbf{y}}_i^l}{\partial \mathbf{y}_i^l}\quad (15)$$

$$= \text{diag} \left(\mathcal{I}_{\{|\mathbf{P}_{\mathbf{g}} \mathbf{g}_i^{l+1}| > b_i^l\}} \right) \mathbf{F}^* \text{diag} \left(\frac{\widehat{\mathbf{k}}^{l*}}{|\widehat{\mathbf{k}}^l|^2 + \zeta_i^l} \right) \mathbf{F},$$

and

$$\frac{\partial \mathbf{z}_i^{l+1}}{\partial \mathbf{k}^l} = \frac{\partial \mathbf{z}_i^{l+1}}{\widehat{\mathbf{g}}_i^{l+1}} \left(\frac{\partial \widehat{\mathbf{g}}_i^{l+1}}{\partial \widehat{\mathbf{k}}^l} \frac{\partial \widehat{\mathbf{k}}_i^l}{\partial \mathbf{k}^l} + \frac{\partial \widehat{\mathbf{g}}_i^{l+1}}{\partial \widehat{\mathbf{k}}^{l*}} \frac{\partial \widehat{\mathbf{k}}_i^l}{\partial \mathbf{k}^l} \right)\quad (16)$$

$$= \text{diag} \left(\mathcal{I}_{\{|\mathbf{P}_{\mathbf{g}} \mathbf{g}_i^{l+1}| > b_i^l\}} \right) \mathbf{F}^* \left[\text{diag} \left(\frac{\zeta_i^l \widehat{\mathbf{y}}_i^l}{(|\widehat{\mathbf{k}}^l|^2 + \zeta_i^l)^2} \right) \mathbf{F}^* - \text{diag} \left(\frac{(\widehat{\mathbf{k}}^{l*})^2 \odot \widehat{\mathbf{y}}_i^l}{(|\widehat{\mathbf{k}}^l|^2 + \zeta_i^l)^2} \right) \mathbf{F} \right],$$

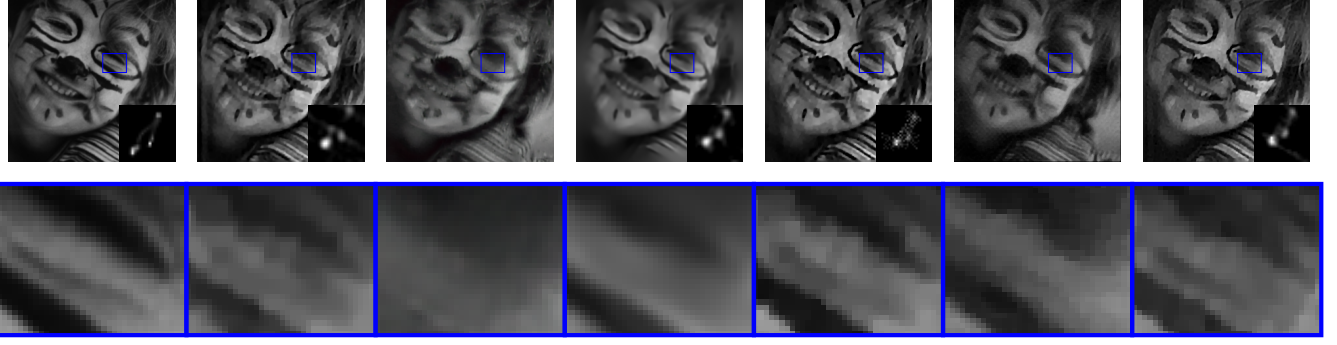
$$\begin{aligned}\frac{\partial \mathbf{k}^{l+1}}{\partial \widehat{\mathbf{k}}^{l+\frac{1}{3}}} &= \frac{\partial \mathbf{k}^{l+1}}{\partial \mathbf{k}^{l+\frac{2}{3}}} \frac{\partial \mathbf{k}^{l+\frac{2}{3}}}{\partial \mathbf{k}^{l+\frac{1}{3}}} \frac{\partial \mathbf{k}^{l+\frac{1}{3}}}{\partial \widehat{\mathbf{k}}^{l+\frac{1}{3}}} \\ &= \frac{\mathbf{I} \left(\mathbf{1}^T \mathbf{k}^{l+\frac{2}{3}} \right) - \mathbf{k}^{l+\frac{2}{3}} \mathbf{1}^T}{\left(\mathbf{1}^T \mathbf{k}^{l+\frac{2}{3}} \right)^2} \text{diag} \left(\mathcal{I}_{\{\mathbf{P}_{\mathbf{k}} \mathbf{k}^{l+\frac{1}{3}} > 0\}} \right) \mathbf{F}^*,\end{aligned}$$

$$\frac{\partial \mathbf{k}^{l+1}}{\partial \mathbf{y}_i^l} = \frac{\partial \mathbf{k}^{l+1}}{\partial \widehat{\mathbf{k}}^{l+\frac{1}{3}}} \frac{\widehat{\mathbf{k}}^{l+\frac{1}{3}}}{\widehat{\mathbf{y}}_i^l} \frac{\widehat{\mathbf{y}}_i^l}{\mathbf{y}_i^l} = \frac{\mathbf{I} \left(\mathbf{1}^T \mathbf{k}^{l+\frac{2}{3}} \right) - \mathbf{k}^{l+\frac{2}{3}} \mathbf{1}^T}{\left(\mathbf{1}^T \mathbf{k}^{l+\frac{2}{3}} \right)^2}.\quad (17)$$

$$\text{diag} \left(\mathcal{I}_{\{\mathbf{P}_{\mathbf{k}} \mathbf{k}^{l+\frac{1}{3}} > 0\}} \right) \mathbf{F}^* \text{diag} \left(\frac{\sum_{i=1}^C \widehat{\mathbf{z}}_i^{l+1*}}{\sum_{i=1}^C |\mathbf{z}_i^{l+1}|^2 + \varepsilon} \right) \mathbf{F},$$

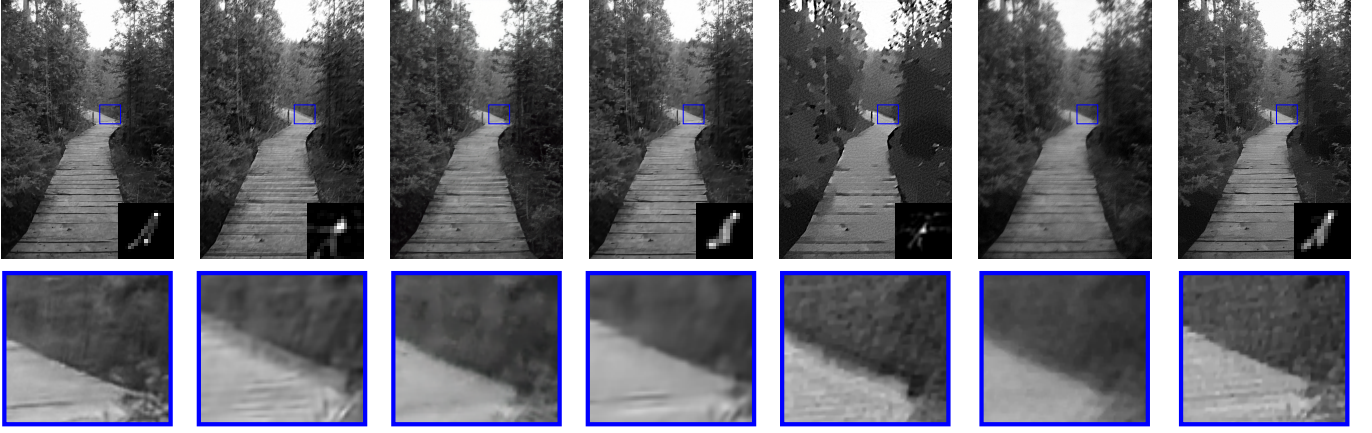
$$\begin{aligned}\frac{\partial \mathbf{k}^{l+1}}{\partial \mathbf{z}_i^{l+1}} &= \frac{\partial \mathbf{k}^{l+1}}{\partial \widehat{\mathbf{k}}^{l+\frac{1}{3}}} \left(\frac{\partial \widehat{\mathbf{k}}^{l+\frac{1}{3}}}{\partial \mathbf{z}_i^{l+1}} \frac{\partial \mathbf{z}_i^{l+1}}{\partial \mathbf{z}_i^{l+1}} + \frac{\partial \widehat{\mathbf{k}}^{l+\frac{1}{3}}}{\partial \widehat{\mathbf{z}}_i^{l+1*}} \frac{\partial \widehat{\mathbf{z}}_i^{l+1*}}{\partial \mathbf{z}_i^{l+1}} \right)\end{aligned}\quad (18)$$

$$= \frac{\mathbf{I} \left(\mathbf{1}^T \mathbf{k}^{l+\frac{2}{3}} \right) - \mathbf{k}^{l+\frac{2}{3}} \mathbf{1}^T}{\left(\mathbf{1}^T \mathbf{k}^{l+\frac{2}{3}} \right)^2} \text{diag} \left(\mathcal{I}_{\{\mathbf{P}_{\mathbf{k}} \mathbf{k}^{l+\frac{1}{3}} > 0\}} \right) \mathbf{F}^*.$$



(a) Groundtruth (b) Perrone *et al.* [23] (c) Nah *et al.* [40] (d) Chakrabarti [28] (e) Xu *et al.* [29] (f) Kupyn *et al.* [66] (g) DUBLID

Fig. 9. Qualitative comparisons on the dataset from [22]. The blur kernels are placed at the right bottom corner. DUBLID generates fewer artifacts and preserves more details than competing state of the art methods.



(a) Groundtruth (b) Perrone *et al.* [23] (c) Nah *et al.* [40] (d) Chakrabarti [28] (e) Xu *et al.* [29] (f) Kupyn *et al.* [66] (g) DUBLID

Fig. 10. Qualitative comparisons on the dataset from [12]. The blur kernels are placed at the right bottom corner.

$$\begin{aligned} & \left[-\text{diag} \left(\frac{\left(\sum_{j=1}^C \widehat{\mathbf{z}}_j^{l+1*} \odot \widehat{\mathbf{y}}_j^l \right) \odot \widehat{\mathbf{z}}_i^{l+1*}}{\left(\sum_{j=1}^C |\widehat{\mathbf{z}}_j^{l+1}|^2 + \varepsilon \right)^2} \right) \mathbf{F} \right. \\ & \left. + \text{diag} \left(\frac{\widehat{\mathbf{y}}_i^l \odot \left(\sum_{j=1}^C |\widehat{\mathbf{z}}_j^{l+1}|^2 + \varepsilon \right) - \left(\sum_{j=1}^C \widehat{\mathbf{z}}_j^{l+1*} \odot \widehat{\mathbf{y}}_j^l \right) \odot \widehat{\mathbf{z}}_i^{l+1}}{\left(\sum_{j=1}^C |\widehat{\mathbf{z}}_j^{l+1}|^2 + \varepsilon \right)^2} \right) \mathbf{F}^* \right], \end{aligned}$$

$$\frac{\partial \mathbf{y}_i^{l-1}}{\partial \mathbf{y}_i^l} = \frac{\partial \mathbf{y}_i^{l-1}}{\partial \widehat{\mathbf{y}}_i^{l-1}} \frac{\partial \widehat{\mathbf{y}}_i^{l-1}}{\partial \widehat{\mathbf{y}}_i^l} \frac{\partial \widehat{\mathbf{y}}_i^l}{\partial \mathbf{y}_i^l} = \mathbf{F}^* \text{diag} \left(\widehat{\mathbf{w}}_i^{l-1} \right) \mathbf{F}. \quad (19)$$

Plugging (14) (15) (16) (17) (18) (19) into (13), we obtain

$$\begin{aligned} \nabla_{\mathbf{k}^l} \mathcal{L} = & \left[\mathbf{F}^* \text{diag} \left(\frac{\zeta_i^l \widehat{\mathbf{y}}_i^l}{\left(|\widehat{\mathbf{k}}^l|^2 + \zeta_i^l \right)^2} \right) - \mathbf{F} \text{diag} \left(\frac{\left(\widehat{\mathbf{k}}^l \right)^2 \odot \widehat{\mathbf{y}}_i^l}{\left(|\widehat{\mathbf{k}}^l|^2 + \zeta_i^l \right)^2} \right) \right] \\ & \mathbf{F}^* \left(\mathcal{I}_{\{|\mathbf{P}_g \mathbf{g}_i^{l+1}| > b_i^l\}} \odot \nabla_{\mathbf{z}_i^{l+1}} \mathcal{L} \right) \end{aligned}$$

$$\begin{aligned} \nabla_{\mathbf{g}_i^l} \mathcal{L} = & \mathbf{F} \text{diag} \left(\frac{\zeta_i^l}{|\widehat{\mathbf{k}}^l|^2 + \zeta_i^l} \right) \mathbf{F}^* \left(\mathcal{I}_{\{|\mathbf{P}_g \mathbf{g}_i^{l+1}| > b_i^l\}} \odot \nabla_{\mathbf{z}_i^{l+1}} \mathcal{L} \right) \\ & + \left[-\mathbf{F} \text{diag} \left(\frac{\left(\sum_{j=1}^C \widehat{\mathbf{g}}_j^l \odot \widehat{\mathbf{y}}_j^{l-1} \right) \odot \widehat{\mathbf{g}}_i^l}{\left(\sum_{j=1}^C |\widehat{\mathbf{g}}_j^l|^2 + \varepsilon \right)^2} \right) \right. \\ & \left. + \mathbf{F}^* \text{diag} \left(\frac{\widehat{\mathbf{y}}_i^{l-1} \odot \left(\sum_{j=1}^C |\widehat{\mathbf{g}}_j^l|^2 + \varepsilon \right) - \left(\sum_{j=1}^C \widehat{\mathbf{g}}_j^l \odot \widehat{\mathbf{y}}_j^{l-1} \right) \odot \widehat{\mathbf{g}}_i^l}{\left(\sum_{j=1}^C |\widehat{\mathbf{g}}_j^l|^2 + \varepsilon \right)^2} \right) \right] \mathbf{F}^* \\ & \left(\frac{1}{1^T \mathbf{k}^{l-\frac{1}{3}}} \mathcal{I}_{\{\mathbf{P}_k \mathbf{k}^{l-\frac{2}{3}} > 0\}} \odot \nabla_{\mathbf{k}^l} C - \frac{\mathcal{I}_{\{\mathbf{P}_k \mathbf{k}^{l-\frac{2}{3}} > 0\}} \mathbf{k}^{l-\frac{1}{3}T}}{\left(1^T \mathbf{k}^{l-\frac{1}{3}} \right)^2} \nabla_{\mathbf{k}^l} \mathcal{L} \right) \end{aligned}$$

$$\begin{aligned}
\nabla_{\mathbf{y}_i^l} \mathcal{L} = & \mathbf{F} \text{diag} \left(\frac{\widehat{\mathbf{k}}^{l*}}{|\widehat{\mathbf{k}}^{l*}|^2 + \zeta_i^l} \right) \mathbf{F}^* \left(\mathcal{I}_{\{|\mathbf{P}_{\mathbf{g}} \mathbf{g}_i^{l+1}| > b_i^l\}} \odot \nabla_{\mathbf{z}_i^{l+1}} \mathcal{L} \right) \\
& + \mathbf{F} \text{diag} \left(\frac{\sum_{i=1}^L \widehat{\mathbf{z}}_i^{l+1*}}{\sum_{i=1}^L |\widehat{\mathbf{z}}_i^{l+1*}|^2 + \varepsilon} \right) \mathbf{F}^* \\
& \left(\frac{1}{1^T \mathbf{k}^{l+\frac{2}{3}}} \mathcal{I}_{\{\mathbf{P}_{\mathbf{k}} \mathbf{k}^{l+\frac{2}{3}} > 0\}} \odot \nabla_{\mathbf{k}^{l+1}} C - \frac{\mathcal{I}_{\{\mathbf{P}_{\mathbf{k}} \mathbf{k}^{l+\frac{2}{3}} > 0\}} \mathbf{k}^{l+\frac{2}{3}T}}{(1^T \mathbf{k}^{l+\frac{2}{3}})^2} \nabla_{\mathbf{k}^{l+1}} C \right) \\
& + \mathbf{F} \text{diag} \left(\widehat{\mathbf{w}}_i^{l-1} \right) \mathbf{F}^* \nabla_{\mathbf{y}_i^{l-1}} \mathcal{L}
\end{aligned}$$

REFERENCES

- [1] D. Kundur and D. Hatzinakos, "Blind image deconvolution," *IEEE Signal Process. Mag.*, vol. 13, no. 3, pp. 43–64, May 1996.
- [2] William Hadley Richardson, "Bayesian-based iterative method of image restoration," *J. Opt. Soc. Am.*, vol. 62, no. 1, pp. 55–59, 1972.
- [3] L. A. Shepp and Y. Vardi, "Maximum Likelihood Reconstruction for Emission Tomography," *IEEE Trans. Med. Imaging*, vol. 1, no. 2, pp. 113–122, Oct. 1982.
- [4] G. R. Ayers and J. Ch. Dainty, "Iterative blind deconvolution method and its applications," *Opt. Lett.*, vol. 13, no. 7, pp. 547–549, 1988.
- [5] Tony F. Chan and Chiu-Kwong Wong, "Total variation blind deconvolution," *IEEE Trans. Image Process.*, vol. 7, no. 3, pp. 370–375, 1998.
- [6] N. Joshi, R. Szeliski, and D. J. Kriegman, "PSF estimation using sharp edge prediction," in *Proc. IEEE Conf. CVPR*, June 2008.
- [7] Qi Shan, Jiaya Jia, and Aseem Agarwala, "High-quality Motion Deblurring from a Single Image," in *Proc. ACM SIGGRAPH*, 2008.
- [8] S. Cho and S. Lee, "Fast Motion Deblurring," in *Proc. ACM SIGGRAPH Asia*, 2009.
- [9] Li Xu and Jiaya Jia, "Two-phase kernel estimation for robust motion deblurring," in *Proc. ECCV*, 2010.
- [10] Dilip Krishnan, Terence Tay, and Rob Fergus, "Blind deconvolution using a normalized sparsity measure," in *Proc. IEEE Conf. CVPR*, 2011.
- [11] L. Xu, S. Zheng, and J. Jia, "Unnatural L0 Sparse Representation for Natural Image Deblurring," in *Proc. IEEE Conf. CVPR*, June 2013.
- [12] L. Sun, S. Cho, J. Wang, and J. Hays, "Edge-based blur kernel estimation using patch priors," in *Proc. IEEE ICCP*, Apr. 2013.
- [13] J. Pan, Z. Hu, Z. Su, and M. H. Yang, "\$L_0\$-Regularized Intensity and Gradient Prior for Deblurring Text Images and Beyond," *IEEE Trans. Pattern Anal. Mach. Intell.*, vol. 39, no. 2, pp. 342–355, Feb. 2017.
- [14] Jian-Feng Cai, Hui Ji, Chaoqiang Liu, and Zuwei Shen, "Framelet-Based Blind Motion Deblurring From a Single Image," *IEEE Trans. Image Process.*, vol. 21, no. 2, pp. 562–572, Feb. 2012.
- [15] Sh. Xiang, G. Meng, Y. Wang, Ch. Pan, and Ch. Zhang, "Image Deblurring with Coupled Dictionary Learning," *Int. J. Comput. Vis.*, vol. 114, no. 2-3, pp. 248–271, Sept. 2015.
- [16] J. Pan, D. Sun, H. Pfister, and M. H. Yang, "Deblurring Images via Dark Channel Prior," *IEEE Trans. Pattern Anal. Mach. Intell.*, vol. PP, no. 99, pp. 1–1, 2018.
- [17] M. Tofghi, Y. Li, and V. Monga, "Blind image deblurring using row-column sparse representations," *IEEE Signal Processing Letters*, vol. 25, no. 2, pp. 273–277, 2018.
- [18] Rob Fergus, Barun Singh, Aaron Hertzmann, Sam T. Roweis, and William T. Freeman, "Removing Camera Shake from a Single Photograph," in *Proc. ACM SIGGRAPH*, New York, NY, USA, 2006.
- [19] A. Levin, Y. Weiss, F. Durand, and W. T. Freeman, "Efficient marginal likelihood optimization in blind deconvolution," in *Proc. IEEE Conf. CVPR*, June 2011.
- [20] S. Derin Babacan, Rafael Molina, Minh N. Do, and Aggelos K. Katsaggelos, "Bayesian Blind Deconvolution with General Sparse Image Priors," in *Proc. ECCV*, Oct. 2012.
- [21] David Wipf and Haichao Zhang, "Revisiting Bayesian blind deconvolution," *J. Mach. Learn. Res.*, vol. 15, no. 1, pp. 3595–3634, 2014.
- [22] A. Levin, Y. Weiss, F. Durand, and W.T. Freeman, "Understanding Blind Deconvolution Algorithms," *IEEE Trans. Pattern Anal. Mach. Intell.*, vol. 33, no. 12, pp. 2354–2367, Dec. 2011.
- [23] Daniele Perrone and Paolo Favaro, "A Clearer Picture of Total Variation Blind Deconvolution," *IEEE Trans. Pattern Anal. Mach. Intell.*, vol. 38, no. 6, pp. 1041–1055, June 2016.
- [24] R. J. Steriti and M. A. Fiddy, "Blind deconvolution of images by use of neural networks," *Opt. Lett.*, vol. 19, no. 8, pp. 575–577, 1994.
- [25] A. Lucas, M. Iliadis, R. Molina, and A.K. Katsaggelos, "Using Deep Neural Networks for Inverse Problems in Imaging: Beyond Analytical Methods," *IEEE Signal Process. Mag.*, vol. 35, no. 1, pp. 20–36, 2018.
- [26] Li Xu, Jimmy SJ Ren, Ce Liu, and Jiaya Jia, "Deep convolutional neural network for image deconvolution," in *Proc. NIPS*, 2014.
- [27] R. Yan and L. Shao, "Blind Image Blur Estimation via Deep Learning," *IEEE Trans. Image Process.*, vol. 25, no. 4, pp. 1910–1921, Apr. 2016.
- [28] Ayan Chakrabarti, "A Neural Approach to Blind Motion Deblurring," in *Proc. ECCV*, Oct. 2016.
- [29] X. Xu, J. Pan, Y. J. Zhang, and M. H. Yang, "Motion Blur Kernel Estimation via Deep Learning," *IEEE Trans. Image Process.*, vol. 27, no. 1, pp. 194–205, Jan. 2018.
- [30] Karol Gregor and Yann LeCun, "Learning fast approximations of sparse coding," in *Proc. ICML*, 2010.
- [31] Y. Lecun, L. Bottou, Y. Bengio, and P. Haffner, "Gradient-based learning applied to document recognition," *Proc. IEEE*, vol. 86, no. 11, pp. 2278–2324, Nov. 1998.
- [32] Z. Wang, D. Liu, J. Yang, W. Han, and T. Huang, "Deep networks for image super-resolution with sparse prior," in *Proc. IEEE ICCV*, 2015.
- [33] K. H. Jin, M. T. McCann, E. Froustey, and M. Unser, "Deep Convolutional Neural Network for Inverse Problems in Imaging," *IEEE Trans. Image Process.*, vol. 26, no. 9, pp. 4509–4522, Sept. 2017.
- [34] Y. Chen and T. Pock, "Trainable Nonlinear Reaction Diffusion: A Flexible Framework for Fast and Effective Image Restoration," *IEEE Trans. Pattern Anal. Mach. Intell.*, vol. 39, no. 6, pp. 1256–1272, 2017.
- [35] Oren Solomon, Regev Cohen, Yi Zhang, Yi Yang, He Qiong, Jianwen Luo, Ruud J. G. van Sloun, and Yonina C. Eldar, "Deep Unfolded Robust PCA with Application to Clutter Suppression in Ultrasound," *arXiv:1811.08252 [cs, stat]*, Nov. 2018.
- [36] Christian J. Schuler, Michael Hirsch, Stefan Harmeling, and Bernhard Scholkopf, "Learning to Deblur," *IEEE Trans. Pattern Anal. Mach. Intell.*, vol. 38, no. 7, pp. 1439–1451, July 2016.
- [37] Y. W. Tai, P. Tan, and M. S. Brown, "Richardson-Lucy Deblurring for Scenes under a Projective Motion Path," *IEEE Trans. Pattern Anal. Mach. Intell.*, vol. 33, no. 8, pp. 1603–1618, Aug. 2011.
- [38] Oliver Whyte, Josef Sivic, Andrew Zisserman, and Jean Ponce, "Non-uniform Deblurring for Shaken Images," *Int. J. Comput. Vis.*, vol. 98, no. 2, pp. 168–186, June 2012.
- [39] Jian Sun, Wenfei Cao, Zongben Xu, and Jean Ponce, "Learning a convolutional neural network for non-uniform motion blur removal," in *Proc. IEEE Conf. CVPR*, 2015.
- [40] Seungjun Nah, Tae Hyun Kim, and Kyoung Mu Lee, "Deep multi-scale convolutional neural network for dynamic scene deblurring," in *Proc. IEEE Conf. CVPR*, 2017, vol. 1, p. 3.
- [41] T. M. Nimisha, A. K. Singh, and A. N. Rajagopalan, "Blur-Invariant Deep Learning for Blind-Deblurring," in *Proc. IEEE ICCV*, Oct. 2017, pp. 4762–4770.
- [42] Shuo Chen Su, Mauricio Delbracio, Jue Wang, Guillermo Sapiro, Wolfgang Heidrich, and Oliver Wang, "Deep Video Deblurring for Hand-held Cameras," in *Proc. IEEE Conf. CVPR*, 2017.
- [43] R. Raskar, A. Agrawal, and J. Tumblin, "Coded Exposure Photography: Motion Deblurring Using Fluttered Shutter," in *ACM SIGGRAPH*, 2006.
- [44] T. S. Cho, A. Levin, F. Durand, and W. T. Freeman, "Motion blur removal with orthogonal parabolic exposures," in *IEEE ICCP*, 2010.
- [45] N. Joshi, S. B. Kang, C. L. Zitnick, and R. Szeliski, "Image Deblurring Using Inertial Measurement Sensors," in *Proc. ACM SIGGRAPH*, 2010.
- [46] J-F. et al. Cai, "Blind motion deblurring using multiple images," *J. Comput. Phys.*, vol. 228, no. 14, pp. 5057–5071, Aug. 2009.
- [47] F. Sroubek and P. Milanfar, "Robust Multichannel Blind Deconvolution via Fast Alternating Minimization," *IEEE Trans. Image Process.*, vol. 21, no. 4, pp. 1687–1700, Apr. 2012.
- [48] Y. Li, M. Tofghi, V. Monga, and Y. C. Eldar, "An algorithm unrolling approach to deep image deblurring," "http://signal.ee.psu.edu/icassp19.pdf", "submitted to 2019 44th IEEE International Conference on Acoustics, Speech, and Signal Processing".
- [49] Rafael C Gonzalez and Richard E Woods, "Digital image processing second edition," *Beijing: Publishing House of Electronics Industry*, vol. 455, 2002.
- [50] W. T. Freeman and E. H. Adelson, "The design and use of steerable filters," *IEEE Trans. Pattern Anal. Mach. Intell.*, vol. 13, no. 9, pp. 891–906, Sept. 1991.
- [51] Jean-Luc Starck, Emmanuel J. Candes, and David L. Donoho, "The curvelet transform for image denoising," *IEEE Trans. Image Process.*, vol. 11, no. 6, pp. 670–684, 2002.

- [52] M. Unser, N. Chenouard, and D. Van De Ville, “Steerable Pyramids and Tight Wavelet Frames in,” *IEEE Trans. Image Process.*, vol. 20, no. 10, pp. 2705–2721, Oct. 2011.
- [53] B. Mailh, S. Lesage, R. Gribonval, F. Bimbot, and P. Vandergheynst, “Shift-invariant dictionary learning for sparse representations: Extending K-SVD,” in *EUSIPCO*, Aug. 2008, pp. 1–5.
- [54] Q. Barthelemy, A. Larue, A. Mayoue, D. Mercier, and J. I. Mars, “Shift amp; 2d Rotation Invariant Sparse Coding for Multivariate Signals,” *IEEE Trans. Signal Process.*, vol. 60, no. 4, pp. 1597–1611, Apr. 2012.
- [55] Y. Wang, J. Yang, W. Yin, and Y. Zhang, “A New Alternating Minimization Algorithm for Total Variation Image Reconstruction,” *SIAM J. Imaging Sci.*, vol. 1, no. 3, pp. 248–272, Jan. 2008.
- [56] U. Schmidt, C. Rother, S. Nowozin, J. Jancsary, and S. Roth, “Discriminative Non-blind Deblurring,” in *IEEE Conf. CVPR*, June 2013.
- [57] Dimitri P Bertsekas, *Constrained optimization and Lagrange multiplier methods*, Academic press, 2014.
- [58] Andrew Blake and Andrew Zisserman, *Visual Reconstruction*, MIT Press, Cambridge, MA, USA, 1987.
- [59] Vinod Nair and Geoffrey E. Hinton, “Rectified linear units improve restricted boltzmann machines,” in *Proc. ICML*, 2010, pp. 807–814.
- [60] Karen Simonyan and Andrew Zisserman, “Very deep convolutional networks for large-scale image recognition,” in *Proc. ICLR*, 2015.
- [61] Diederik P. Kingma and Jimmy Ba, “Adam: A method for stochastic optimization,” in *Proc. ICLR*, 2015.
- [62] Xavier Glorot and Yoshua Bengio, “Understanding the difficulty of training deep feedforward neural networks,” in *Proc. ICAIS*, Mar. 2010.
- [63] P. Arbelaez, M. Maire, C. Fowlkes, and J. Malik, “Contour Detection and Hierarchical Image Segmentation,” *IEEE Trans. Pattern Anal. Mach. Intell.*, vol. 33, no. 5, pp. 898–916, May 2011.
- [64] T-Y. Lin, M. Maire, S. Belongie, J. Hays, P. Perona, D. Ramanan, P. Dollár, and C.L. Zitnick, “Microsoft coco: Common objects in context,” in *Proc. ECCV*. Springer, 2014, pp. 740–755.
- [65] Kaiming He, Xiangyu Zhang, Shaoqing Ren, and Jian Sun, “Deep Residual Learning for Image Recognition,” in *Proc. IEEE Conf. CVPR*, June 2016, pp. 770–778.
- [66] O. Kupyn, V. Budzan, M. Mykhailych, D. Mishkin, and J. Matas, “Deblurgan: Blind motion deblurring using conditional adversarial networks,” in *Proc. IEEE Conf. CVPR*, June 2018.
- [67] Ian Goodfellow, Jean Pouget-Abadie, Mehdi Mirza, Bing Xu, David Warde-Farley, Sherjil Ozair, Aaron Courville, and Yoshua Bengio, “Generative adversarial nets,” in *Proc. NIPS*, 2014, pp. 2672–2680.
- [68] Zhou Wang, A.C. Bovik, H.R. Sheikh, and E.P. Simoncelli, “Image quality assessment: from error visibility to structural similarity,” *IEEE Trans. Image Process.*, vol. 13, no. 4, pp. 600–612, Apr. 2004.
- [69] J. Kim, J. K. Lee, and K. M. Lee, “Accurate Image Super-Resolution Using Very Deep Convolutional Networks,” in *Proc. IEEE Conf. CVPR*, June 2016, pp. 1646–1654.
- [70] D. Martin *et al.*, “A database of human segmented natural images and its application to evaluating segmentation algorithms and measuring ecological statistics,” in *Proc. IEEE ICCV*, July 2001.
- [71] R. Khler *et al.*, “Recording and playback of camera shake: Benchmarking blind deconvolution with a real-world database,” in *Proc. ECCV*. 2012, pp. 27–40, Springer.